SUBCELLULAR TRAFFICKING WITH SINGLE MOLECULE MICROSCOPY IN THREE DIMENSIONS

A Dissertation

by

SUNG YONG YOU

Submitted to the Office of Graduate and Professional Studies of
Texas A&M University
in partial fulfillment of the requirements for the degree of

DOCTOR OF PHILOSOPHY

Chair of Committee,	Raimund J. Ober
Co-Chair of Committee,	Alvin T. Yeh
Committee Members,	Kristen Maitland
	E. Sally Ward
Head of Department,	Mike McShane

December 2020

Major Subject: Biomedical Engineering

ABSTRACT

Recently, single-molecule microscopy techniques have increasingly been used to study the subcellular trafficking of biomolecules due to their nanometer-scale resolution and multicolor imaging capabilities. These techniques rely on the accurate localization of single molecules. Therefore, calibrating the microscope and its optical components is important in the field of single-molecule microscopy because accurate and careful calibration helps guarantee a high level of accuracy that is often required in the analysis of single-molecule image data. In this study, we develop an approach for calibrating single-molecule microscopy systems at the nanometer scale. Using this approach, we assess the performance of single-molecule microscopes and their optical elements by detecting geometric aberrations in the emission light path.

Another contribution that we make in this dissertation is that we develop a method for evaluating and optimizing remote-focusing multifocal plane microscopy (rMUM). Generally, rMUM is an imaging technique that allows the acquisition of single-molecule trajectories in three dimensions while simultaneously acquiring z-stack images of the cellular context. However, in practical implementations of rMUM, it is challenging to evaluate and optimize rMUM data with a high accuracy because of the complex image data set generated by the rMUM experiments. Therefore, in this study, we develop an experimental protocol for evaluating and optimizing the performance of rMUM. This protocol relies on determining the localization accuracy of single molecules, measuring

the spatial registration accuracy, and correcting for the focal shift due to the refractive index mismatch.

DEDICATION

To my family

ACKNOWLEDGEMENTS

I wish to express my deepest gratitude to Professors Raimund J. Ober and E. Sally Ward for their time, support, and guidance during my doctoral studies. I offer thanks to Professor Alvin T. Yeh for his professional guidance and for taking his time to serve on the co-chair of my committee. I also want to thank Professor Kristin Maitland for generously offering her time and support.

Additionally, I am grateful to all former and current members of the Ward Ober Lab. In particular, I would like to thank Dr. Dongyoung Kim for helping me to get started with optical microscopy experiments. I would also like to acknowledge Dr. Jerry Chao for his invaluable feedback on my manuscripts and Sreevidhya Ramakrishnan for research collaboration during my Ph.D. Special thanks to Wooseok Kim, Anish V. Abraham, David D. Kim, Drs. Edward A.K. Cohen, Jeffrey Kang, and Ramraj Velmurugan, for their generous support during my Ph.D.

Nobody has been more important to me in the pursuit of this dissertation than the members of my family. First and foremost, I would like to thank my parents for their endless love and continued support for my Ph.D. More importantly, I wish to thank my wife, Hyunsook Jung, and my two children, Claire and Colin. They have been extremely supportive of me and have made countless sacrifices to help me get to this point.

October 14, 2020

CONTRIBUTORS AND FUNDING SOURCES

Contributors

This work was supported by a dissertation committee consisting of Professors Raimund J. Ober (chair) previously of the Department of Biomedical Engineering at Texas A&M University and currently of the Department of Imaging and Biomedical Engineering at the University of Southampton; Professor Alvin T. Yeh (co-chair) and Professor Kristen Maitland of the Department of Biomedical Engineering at Texas A&M University; and Professor E. Sally Ward of the Department of Molecular Immunology at the University of Southampton.

The accepted manuscript reprinted in Section 2 was authored by the student, Dr. Jerry Chao of Astero Technologies LLC, Dr. Edward A. K. Cohen of the Department of Mathematics at Imperial College London, Professor Raimund J. Ober, and Professor E. Sally Ward. The experiments detailed in Section 2 were designed in part by the student in collaboration with Professor Raimund J. Ober. The data analysis depicted in Section 2 was devised in part by the student in collaboration with Dr. Edward A. K. Cohen and Professor Raimund J. Ober. The draft of the manuscript was prepared in part by the student in collaboration with Dr. Jerry Chao and Professor Raimund J. Ober.

The prototype presented in Section 3 was conceptualized in part by Dr. Dongyoung Kim and Professor Raimund J. Ober. The data acquisition described in Section 3 was performed by Sreevidhya Ramakrishnan of the Department of Biomedical Engineering at Texas A&M University. The data analysis depicted in Section 3 was devised in part by the student in collaboration with Dr. Jerry Chao. The software used in Section 3 was prepared in part by the student in collaboration with Dr. Jerry Chao and Anish V. Abraham of the Department of Biomedical Engineering. The writing and reviewing of Section 3 were conducted in part by the student in collaboration with Sreevidhya Ramakrishnan and Dr. Jerry Chao.

All other work conducted for the dissertation was completed independently by the student.

Funding Sources

This work was supported in part by a grant by the National Institutes of Health (R01 GM085575, R44 GM121113) and the Wellcome Trust (206411/Z/17/Z).

TABLE OF CONTENTS

LIST OF FIGURES

LIST OF TABLES

Page

1. INTRODUCTION

Optical microscopes are an essential tool in biological research. Since the invention of the first compound microscope by Leeuwenhoek three centuries ago, significant advancements have been made in this field [1]. One of the main discoveries that boosted the popularity of optical microscopes was fluorescence microscopy, which was introduced in the 19th century by David Brewster. A fluorescence microscope is an optical microscope that uses fluorescent labels, such as quantum dots (QDs), fluorescent proteins (FPs), and organic dyes [2]. These fluorescent labels can be attached to the proteins of interest with high specificity in a non invasive manner, providing a high-intensity contrast in the microscopic image [3]. Such advantages make fluorescence microscopy an attractive tool for studying molecular dynamics in living cells.

However, there are two significant reasons why classical fluorescence microscopy limits the study of interactions between individual protein molecules in cells. The first reason is that the diffraction properties of light limit the optical resolution to several hundred nanometers, a phenomenon that was fully described and formularized by Ernst Abbe in 1873 [4]. The second reason is that classical fluorescence microscopy often requires a considerable number of fluorescent molecules to produce a detectable signal, as each fluorescent molecule emits only a limited number of photons [5]. These two reasons can hamper the discovery of heterogeneous molecular processes at the level of individual molecules.

1.1. Single-molecule microscopy

Single-molecule microscopy is an imaging technique that allows the detection of single fluorescent molecules [5]. In 1989, William E. Moerner and L. Kador performed single-molecule detection in condensed matter for the first time [6]. In classical fluorescence microscopy, generally, the signal emitted by each single fluorescent molecule is typically too low to be detected above the noise level of the detector. In the 1990s, highly sensitive cameras capable of detecting a single molecule were developed, paving the way for single-molecule microscopy. In 1990, Michel Orrit succeeded in detecting the emitted fluorescence at room temperature [7].

One of the main discoveries that popularized fluorescence microscopy was the labeling technology based on green fluorescent protein (GFP). Notably, GFP was first isolated from a jellyfish by Osamu Shimomura in 1962 [8]. Generally, the ability to incorporate the expression of an FP into a protein of interest in living cells allows studying biological processes in a minimally perturbative and a highly specific manner.

Over the last two decades, single-molecule experiments have been widely used in the field of biology for a broad range of applications [9]. Two of the essential types of single-molecule experiments are localization-based super-resolution imaging and single-molecule tracking. Both techniques rely on a concept that allows determining the position of an individual molecule with high precision [9], and they are discussed in more detail below.

1.2. Single-molecule tracking experiment

Studying the molecular dynamics is of fundamental importance for understanding cellular processes. In the 1970s, Axelrod first introduced fluorescence recovery after photobleaching (FRAP) to study the kinetics of fluorescent molecules on the cell surface [10]. This method allows measuring the averaged behavior of an ensemble of molecules, such as diffusion coefficients [11]. However, it is essential to study the molecular dynamics at the single-molecule level to obtain a detailed understanding of many biological processes.

Single-molecule tracking experiments can provide important information about the subcellular trafficking pathway of individual molecules within cells. One of the examples is the tracking of IgG and FcRn molecules. Generally, IgG transport in cells is essential for effective humoral immunity, and FcRn plays a significant role in IgG transport [12]. Therefore, understanding the intracellular trafficking pathway of IgG and FcRn is critical for investigating the mechanisms that maintain the IgG level in the body [13–15].

Three critical issues need to be considered through in single-molecule tracking experiments. The first one is the crowding problem, which occurs when molecules are placed too close to each other, making them indistinguishable when imaged by an optical microscope. This problem can be solved by labeling only a few representative molecules rather labeling all of them.

Photobleaching of fluorescent labels is one of the most severe problems in single-molecule tracking. Most organic dyes and FPs are susceptible to photobleaching, a phenomenon in which a fluorophore loses its fluorescence after a certain number of excitation and emission cycles [16]. Moreover, the rate of photobleaching strongly depends on the excitation power. This is particularly critical in live-cell microscopy experiments given the tradeoff between the need to minimize the photobleaching of organic dyes or FPs for long-term imaging and the need to obtain images with a high signal-to-noise ratio using high excitation power [17]. Given their high photostability and brightness, QDs are generally ideal for these applications. Therefore, when using QDs, cells can be imaged for longer times and at reduced laser power. However, some issues still need to be overcome when QDs are used in single-molecule experiments, such as non-specific binding and QD blinking [18–20].

In addition, highly sensitive cameras with high frame rates are often required to capture the rapid dynamics of individual molecules. The location of a molecule in consecutive images is usually estimated by fitting a PSF model (e.g., 2D Gaussian or Airy profile) to the region of the image that contains the molecule [21]. Each trajectory is then obtained by connecting the estimated position of the molecule in consecutive images and is often quantified by analyzing the mean squared displacement [22]. This approach can differentiate between different diffusion behaviors, such as Brownian diffusion, directed motion, and confined motion [23–25].

1.3. Techniques for single-molecule imaging

Widefield imaging technique has been widely used in live-cell imaging applications, for imaging of multiple single molecules in specimens. This technique allows capturing an entire specimen at once, thereby providing spatial information with fast temporal resolution [26]. Standard widefield fluorescence microscopes usually consist of a light source, an objective lens, optical filters (e.g., excitation, emission, and dichroic filters), a microscope, and a camera. All fluorophores in the sample are illuminated with light of a specific wavelength, and the light emitted from these fluorophores is captured by a camera that supports high-sensitivity imaging with high frame rates, such as charge-coupled devices (CCDs), electron-multiplying charge-coupled devices (EMCCDs), or scientific complementary metal-oxide semiconductors (sCMOSs) [27]. Notably, the type of camera used needs to be chosen with great care. Generally, sCMOS cameras can provide much faster frame rates for imaging acquisition than those of CCD and EMCCD cameras. However, since the offset and readout noise levels vary from one pixel to another, it is difficult to calibrate the camera [28]. In addition, EMCCD cameras should be used only when the photon count per pixel is very low (i.e., low-light imaging) [29].

Sanderson [30] described the basic principle of widefield fluorescence imaging system as follows. First, the excitation light by a laser, lamp, or light-emitting diode (LED) reaches the specimen through an objective lens after being reflected by a dichroic filter. However, before being reflected by the dichroic filter, the excitation light must pass through an excitation filter so that only light with the desired wavelength reaches the specimen. Then, the light emitted from the fluorophores in the specimen is collected by an objective lens, passes through a dichroic filter, and is focused onto a camera. Emission filters are often used to ensure that only light with the desired wavelength reaches the camera and to avoid scattered light and other background light.

A major problem in widefield microscopy is the significant background noise due to out-of-focus fluorescence. Therefore, In 1980s, total internal reflection fluorescence microscopy (TIRFM) was first introduced to overcome the limitations in measuring the molecular interactions of surface-associated fluorescent molecules [31]. Generally, TIRFM is a widefield imaging technique that selectively excites part of the cells (close to the cover glass) using an evanescent wave generated by focusing a light source on the back focal plane of an objective lens. This significantly decreases the noises due to the out-of-focus fluorescence in comparison to conventional widefield microscopy, providing excellent signal-to-noise ratios near the excitation plane (~200 nm) [32].

Although TIRFM is considered very suitable for imaging subcellular trafficking events close to the plasma membrane, it has some limitations in studying subcellular dynamics in three dimensions (3D). Therefore, several approaches have been introduced to overcome these limitations. One of these approaches is based on sequentially scanning a sample along with the optical axis. However, this approach has speed related limitations for studying fast dynamics in cells. Another approach is based on encoding 3D information into a point spread function (PSF) profile, also called PSF engineering, such as astigmatism [33,34] and double helix [35,36]. Compared to these techniques, multifocal plane microscopy (MUM) [37–39] offers significant advantages for implementing single-molecule imaging. For example, MUM can be easily combined with other configurations to overcome or improve the challenges of the current configurations. Generally, MUM is a widefield microscopy technique that allows simultaneously collecting images at different focal planes within a specimen [40]. Earlier, we implemented a MUM configuration that enables 3D subcellular trafficking of single Transferrin molecules conjugated with QDs in a 10 μm thick live cell [38].

1.4. Challenges of single-molecule microscopy

1.4.1. Calibration of single-molecule imaging systems

Accurate localization of individual molecules plays a critical role in the applications of single-molecule tracking and localization-based super-resolution imaging. Recent studies [41,42] have shown that the accurate localization of single molecules is routinely achievable in single-molecule microscopy experiments. This leap in resolution is considered promising and may provide novel insights into the study of intracellular trafficking of individual molecules at the nanometer level. Notably, this technique has been used to obtain quantitative information at the nanoscale about the molecular processes within a cell [43,44].

Generally, when imaging at the level of single molecules, a well-calibrated microscope needs to achieve highly accurate measurements of the quantities of interest. Various studies have shown that the performance of a microscope can be assessed with commercially available calibration samples and analysis tools [45,46]. However, these methods lack accuracy because of the simplistic assumptions made about the calibration sample. Calibration with nanometer-level accuracy is critical for single-molecule microscopy, as even a slightly miscalibrated microscope can result in significant misinterpretations of data. Moreover, the current methods do not provide an accurate evaluation of dichroic filters and objective lenses, even though the geometric and chromatic aberrations introduced by these optical elements can cause severe issues in multicolor imaging applications.

1.4.2. Imaging of a single-molecule trajectory and its 3D cellular context

Generally, single-molecule tracking experiments in 3D are considered to be promising and may provide novel insights into the study of intracellular trafficking of single molecules in live cells [37,47]. As mentioned earlier, MUM is an optimal imaging technique that can accurately estimate the 3D location of single molecules over a large depth at a high temporal resolution [38]. However, this technique has an issue: the visualization of detailed subcellular structures in 3D with which the single molecules interact. Therefore, this technique is considered to be limited in its usefulness as it provides little or no information about the cellular context in which the dynamics occur. Generally, the trajectory of a single molecule is of little use if the context of the subcellular compartments within which the trajectories occur cannot be determined.

An initial prototype of remote-focusing multifocal plane microscopy (rMUM) has been established by incorporating both MUM and a remote-focusing configuration [48,49]. Specifically, the MUM-module images the 3D trajectories of single molecules, and the remote-focusing module performs sequential scanning of the specimen without moving the objective lens or the sample. This imaging system allows imaging single molecules at high spatial and temporal resolutions and imaging detailed cellular structures in which molecules interact. However, currently, there is a lack of methods for evaluating and optimizing the performance of rMUM, such as localization accuracy or precision of single molecules and spatial registration error between r- and MUM-modules. Multicolor imaging experiments using rMUM produce very complex multi-dimensional data sets, which require accurate and careful calibration, control experiments, and data processing approaches.

1.5. Overview of the dissertation

This dissertation is organized as follows. In Section 2, we develop a new method for calibrating a single-molecule microscopy system at the nanometer scale. The performance of a microscope is evaluated with nanometer-level accuracy by determining the deviations between the measured locations of points in the imaged calibration sample and their corresponding reference locations. Furthermore, to provide support for multicolor imaging, some procedures are included to accurately evaluate the geometric aberrations caused by dichroic filters and the axial chromatic aberrations introduced by objective lenses.

In Section 3, we introduce a calibration approach to evaluate the performance of rMUM. This method entails an experimental pipeline that includes control data acquisition/arrangement, spatial registration, 3D single-molecule localization, and focal shift correction.

2. A MICROSCOPE CALIBRATION PROTOCOL FOR SINGLE-MOLECULE MICROSCOPY[*]

2.1. Introduction

Single-molecule wide-field microscopy experiments have been widely used for a broad range of investigations in cell-biological studies [9]. Two of the most important types of such single-molecule experiments are single-molecule tracking and localization-based super-resolution experiments. Single-molecule tracking experiments hold the promise to reveal fundamental insights into dynamic molecular processes in live cells that remain difficult to uncover using classical microscopy approaches [13,34,50,51]. Localization-based super-resolution microscopy can yield quantitative information on the spatial distribution of a molecule of interest and the spatial characteristics of cellular structures smaller than the diffraction limit [52–55]. Both types of experiments importantly depend on the estimation of the position of single molecules with a low level of uncertainty (i.e., a small variance or standard deviation) [56].

Localization of single molecules with statistical uncertainties of tens of nanometers is routinely achievable in single-molecule microscopy [41,57], and sub-nanometer uncertainty is even possible when using fluorophores that emit large numbers of photons [58,59]. Being able to achieve sub-nanometer uncertainty is critical for our current

---

[*] This chapter contains the content of an article that is accepted for publication: S. You, J. Chao, E. A. K. Cohen, R. J. Ober, and E. S. Ward, "A microscope calibration protocol for single-molecule microscopy," Opt. Express (2020)

purposes, as we seek to assess the performance of microscopes and optical components by determining differences in the positional estimates of imaged point sources that will typically be on the order of nanometers.

The complexity of advanced microscopy setups, optical imperfections, and possible misalignments of mirrors or lenses can all contribute to geometric aberrations in the image produced by a microscope. Errors due to such non-ideal conditions can lead to erroneous answers to biological questions, even when they are on the nanometer scale. For example, when imaging the dynamics of a single molecule that interacts with an endosome, the position of a single molecule may be determined to be inside rather than outside of the endosome, or vice versa, when the localization error is on the order of only nanometers. Errors of this nature can obviously lead to vastly different interpretations of the biological phenomenon. Therefore, to ensure that data of reliably good quality is produced, the performance of the imaging system must be routinely assessed prior to performing single-molecule imaging experiments. This assessment requires defined samples that can be used as standards and calibration methods that are suited for single-molecule localization microscopy. The calibration methods should be system-independent and yield reproducible results, such that the same standards can be used to calibrate different microscopes.

Several calibration standards have been introduced over the years to characterize the performance of an imaging system, including ones that utilize fluorescent beads [60,61] and DNA origami [62,63]. In approaches that make use of beads, the samples are typically prepared by mounting randomly distributed small fluorescent beads (0.1 μm in diameter) onto the cover glass. For example, 0.1 µm TetraSpeck fluorescent beads (Thermo Fisher Scientific) are one of the common standards for fluorescence microscopy and have four well-separated pairs of excitation and emission peaks located at 350/440 nm (blue), 505/515 nm (green), 575/585 nm (orange) and 655/685 nm (dark red). Their ability to produce fluorescence of different colors makes them a particularly good calibration standard for multicolor applications. However, fluorescent beads can form aggregates, leading to quenching and altered spectroscopic properties. An approach using beads also has limited sampling uniformity in terms of the size and distribution of the beads. Unlike with fluorescent beads, with DNA origami the distribution of the fluorophores can be controlled on the sub-micrometer level. However, the emitter intensity and stability are limited and, furthermore, it may be challenging to create a DNA origami sample occupying a field of view that is large enough to capture at least an entire biological cell of interest (i.e., at least tens of micrometers per lateral dimension).

To overcome the various limitations of approaches that use beads or DNA origami, in recent years techniques have been developed to create slides imprinted with defined patterns for system calibration. For example, Argolight uses a laser to induce into glass substrates fluorescent materials that are stable and have a broadband emission spectrum. An example of an Argolight slide contains different fluorescent patterns in two and three dimensions, the elementary structure of which is an empty cylinder with a diameter of about 0.7 µm. A second technique is the lithography system used by Miraloma Tech to produce calibration slides containing defined patterns. A particularly useful pattern consists of an array of regularly spaced sub-wavelength-sized apertures, allowing for uniform sampling of the imaging field. These apertures are empty and imaged using trans-illumination. Hence the imaging of these slides is not affected by fluorophore photobleaching and can produce extremely high signal-to-noise ratio images even with short exposure times.

Recent studies have used arrays of regularly spaced points (i.e., small apertures or fluorescent features) or other patterns or features to evaluate the performance of fluorescence microscopes in terms of lateral resolution, field distortion, chromatic aberration, etc. In [64], arrays of small apertures, fabricated using electron-beam lithography and filled with fluorescent dyes, are used to measure field-dependent variations in the three-dimensional (3D) point spread function of a microscope, which have direct implications on the accuracy of the 3D localization of single molecules. In [65], laser-written fluorescent patterns are utilized for evaluating microscope properties such as illumination uniformity and chromatic alignment. In [66], arrays of circular apertures, fabricated using electron-beam lithography, are used to determine the field curvature, assess chromatic aberration, and evaluate other aspects of a microscope.

We will similarly make use of an array of sub-wavelength-sized apertures in this study. The basis of our microscope calibration method is the evaluation of geometric aberrations by way of determining the difference between the true and the measured positions of the apertures. An important issue we take into account is that there can be manufacturing errors associated with the positions and sizes of the apertures. Our method determines the true aperture positions as a set of reference positions, as relying on the nominal aperture positions would make it difficult to determine whether the geometric aberrations observed in the acquired images are due to defects in the optical system or manufacturing errors in the calibration sample.

Recently, simultaneous multicolor single-molecule tracking has been widely used for the observation of the fast dynamics of individual molecules in living cells [13,67,68]. For these experiments, the imaging system requires the use of dichroic filters to separate signals of different colors. However, previous studies have not evaluated how much the image quality is affected by geometric aberrations due to the surfaces of the dichroic filters being insufficiently flat. In addition, few methods have been introduced to evaluate the objective lens in terms of the chromatic aberration that it introduces.

Therefore, the calibration method that we present here is optimized for multicolor single-molecule microscopy. This method couples the use of a lithographically fabricated aperture array with novel analysis algorithms to evaluate the performance of the microscope and its optical components with high accuracy.

The proposed method comprises two major components. The first component concerns the assessment of the performance of a microscope by determining the level of geometric aberration in its optical path. As the extent of the aberration is reflected in the deviation of the imaged positions of microscopic apertures in the calibration sample from their true positions, the key here, as mentioned above, is to establish a set of accurately determined reference aperture positions that serve as a benchmark for comparison in subsequent calibrations of a microscope using the same sample. The approach, therefore, entails procedures for the accurate estimation of imaged aperture positions and the determination of the similarity between a given set of aperture position estimates and the reference aperture positions.

The second component of the proposed calibration method comprises approaches for evaluating two critical microscope components, namely the objective lens and the dichroic filter. The quality of the objective lens is evaluated based on how well it corrects for chromatic aberration along the optical axis. This assessment is important because there is no guarantee that even apochromat objectives will be able to fully correct for the aberration over a wide spectral range. The performance of the dichroic filter is evaluated by investigating the deviation between corresponding aperture positions estimated from images simultaneously acquired of the filter’s transmitted and reflected light paths. This type of evaluation is of particular importance because it is often the case that suboptimal properties of a dichroic filter lead to distortions in the light that it reflects.

The proposed calibration method is supported by a core set of analysis tools for carrying out a number of important tasks. These tasks comprise the determination of the in-focus position of a 3D data set, the registration of images in two dimensions, the estimation of the position of an aperture, the assessment of the horizontality of the microscope stage and calibration sample, and the quantitative comparison of two data sets.

To demonstrate the evaluation of the performance of a microscope, we apply our calibration method to both a microscope of poor quality (one with a damaged objective thread adapter) and a microscope of good quality. Our results show that our method is capable of distinguishing between the two microscopes in terms of the level of geometric aberration.

In addition, we apply our method to an apochromat objective lens to evaluate its axial chromatic aberration over a wide spectral range. We also demonstrate the ability of our method to distinguish between dichroic filters that differ in terms of their flatness.

The proposed method enables meaningful and repeatable calibration data acquisitions that are reproducible across different microscopes. Also, our approach provides useful insights into the selection of an appropriate microscope and suitable optical elements for a given application. It allows researchers, ranging from novice microscope users to expert microscopists, to evaluate their microscopes and optical elements with high accuracy.

2.2. Methods

We describe in this section the type of sample, instrumentation, and data that are required by our calibration method, as well as the specific implementations that are used in Section 2.3 to demonstrate the method. We also detail here the protocols that comprise our method, including a core set of analysis tools on which the protocols rely. Although it is not a part of the calibration method, we additionally present here a procedure to simulate data sets for the investigation of a measure that we introduce for the comparison of two data sets.

2.2.1. Calibration sample

A NanoGrid slide (Miraloma Tech, LLC) is used as a calibration standard for the microscope performance evaluation. The slide consists of a 20 by 20 array of sub-wavelength-sized apertures with a regular spacing of 4 μm between adjacent apertures. The apertures, which we will also refer to as holes, are approximately 200 nm in diameter.

The numbers for the spacing and diameter are taken from specifications provided by the manufacturer. Of the 20 by 20 array of holes, only the center 10 by 10 holes are used for the proposed analyses (except for the determination of the in-focus image of a z-stack (Section 2.2.4), which is carried out using the whole image). The field of view corresponding to the center 10 by 10 holes is large enough to capture a single cell of interest in its entirety (which is typically all that is needed in single-molecule imaging), and yet small enough to help speed up the rate of image acquisition.

2.2.2. Microscope setups

We use the following three microscope configurations for the current study. The first microscope configuration ("microscope 1") consists of a standard inverted microscope (Axio Observer A1, Carl Zeiss) and an EMCCD camera (iXon Ultra, Andor) operated in CCD readout mode. The camera exposure time is set to 0.1 s. The plan-apochromatic objective lens (Cat. No. 420782-9900-000, Carl Zeiss) has a 63× magnification and a numerical aperture of 1.4 and is used with an immersion medium with an index of refraction of 1.51. A piezo objective positioner (P-721, Physik Instrumente) is used to translate the objective lens in the z direction. This device has a positioning repeatability (i.e., the precision for attaining a target position under identical conditions) of ±5 nm. A microscope objective thread adapter (Cat. No. 000000-1095-168, Carl Zeiss) is installed between the objective lens and the piezo objective positioner. This adapter allows microscope objectives with RMS (Royal Microscopical Society) objective mounts to be used on piezo objective positioners with M27 (metric 27-millimeter) threads. To provide an example of a microscope with geometric aberrations, the adapter that is installed is replaced with one whose thread is damaged. The damaged thread causes the objective lens to deviate from its alignment with the optical axis, resulting in aberrations in the image formed.

The second microscope configuration ("microscope 2") consists of a standard inverted microscope (Axio Observer Z1, Carl Zeiss) and a CCD camera (ORCA-ER, Hamamatsu Corporation). The camera exposure time is set to 0.2 s. The plan-apochromatic objective lens (Cat. No. 420782-9900-000, Carl Zeiss) has the same magnification and numerical aperture as the objective lens for the first setup and is used with the same immersion medium. A motorized focus drive included in the microscope stand is used to translate the objective lens along the optical axis. For chromatic aberration analysis, microscope 2 is equipped with filter sets for FITC (Filter set 38, Carl Zeiss), Cy3 (Filter set 43, Carl Zeiss), and Cy5 (Filter set 50, Carl Zeiss).

The third microscope configuration ("microscope 3") is assembled by adding an emission image splitter (Cat. No. 1058640000, Carl Zeiss) to microscope 1. Two identical EMCCD cameras (iXon Ultra, Andor), both operated in CCD readout mode, are connected to the output ports of the image splitter unit. The exposure time is set to 0.1 s for each camera. For the evaluation of dichroic filters, either a standard flatness dichroic filter (FF625-SDi01, Semrock Inc) or an improved flatness dichroic filter (FF560-FDi01, Semrock Inc) is mounted in a filter cube and placed in the image splitter unit.

Briefly, after adding the image splitter to the microscope and attaching the two cameras, the following procedure is performed to align the in-focus positions of the two cameras.

A filter cube with a 50:50 beam splitter is inserted into the image splitter, and a NanoGrid slide is positioned so that its image is placed in the center of the field of view of the camera in the transmitted light path. If necessary, the xy position of the camera in the reflected light path is then adjusted (using position adjustment knobs that are part of the image splitter) so that the image of the slide is also centered in its field of view. To check whether the two cameras share a focal plane, z-stacks of the NanoGrid sample are simultaneously acquired using the cameras, and the procedure of Section 2.2.4 is used to analyze each z-stack to determine the in-focus position of its respective camera. If the in-focus positions of the two cameras do not match well, then the z position of the camera in the reflected light path is adjusted as needed, again using the adjustment knobs. The z-stack acquisition and analysis are repeated until the two cameras are found to share a focal plane.

The image splitter used in microscope 3 is a discontinued product. A similar product that could be used is the Double Adapter Duolink (Cat. No. 426143-9000-000, Carl Zeiss) [69].

In all three microscope setups, the NanoGrid calibration slide is trans-illuminated with a light-emitting diode (LED) (M810L3-C4, Thorlabs Inc). Also, the mechanical stage (Mechanical stage 130x85 R/L with short coaxial drive, Carl Zeiss) is equipped with a mounting frame (Universal Mounting Frame K, Carl Zeiss) that can hold a petri dish (max. diameter 68 mm) or a sample slide (max. length 120 mm). The mounting frame can be detached from the stage and rotated 180 degrees.

2.2.3. Acquisition of calibration data

In this paper, three types of calibration data sets are utilized. The first type (“calibration data set 1”) consists of a z-stack of the NanoGrid slide, the second type (“calibration data set 2”) comprises multicolor z-stacks of the slide, and the third type (“calibration data set 3”) consists of 200 in-focus images of the slide.

Calibration data set 1 is acquired as follows. The aperture array on the calibration slide is placed at the center of the imaging field. A z-stack is then acquired by moving the objective lens along the optical axis to obtain a series of images centered about the visually determined in-focus position. More specifically, the z-stack is obtained by moving the objective lens with a piezo nanopositioner or a motorized focus drive in 50-nm steps and acquiring an image at each position of the objective lens. Calibration data set 2 is acquired using the same procedure, except an image of each of the color channels is taken per z-step using a motorized filter cube turret.

Calibration data set 3 is acquired as follows. A z-stack is first acquired using the procedure for the acquisition of calibration data set 1. The in-focus frame number of the z-stack is determined as described in Section 2.2.4, and the in-focus position of the objective lens is obtained as the product of this frame number and the step size used to acquire the z-stack. The objective lens is then moved to the in-focus position, and 200 images are acquired sequentially.

2.2.4. Determination of the in-focus position of a z-stack

The Brenner gradient method [70,71] is used to determine which image amongst a z-stack of images (i.e., from calibration data set 1 or 2) is closest to being in-focus. The method is a computationally efficient edge detector that measures the intensity difference between a pixel and a neighboring pixel. When plotted as a function of the frame number in a z-stack, the Brenner gradient exhibits a sharp peak at the in-focus position and drops rapidly away from the in-focus position. For each image in a z-stack, the Brenner gradient is computed as

$$F_{Brenner} = \sum_{i=1}^{M-m} \sum_{j=1}^{N} [I(i,j) - I(i+m,j)]^2 \,,$$

where $I(i,j)$ is the intensity of pixel (i,j), M and N are the height and width of the image in pixels, and $m = 2$. Each Brenner gradient value $F_{Brenner}$ is normalized using the formula

$$F_{norm} = (F_{Brenner} - F_{min}) \times \frac{1}{F_{max} - F_{min}},$$

where F_{min} and F_{max} are the smallest and largest of the gradients calculated for all images in the stack. The Brenner gradient for each frame in the z-stack is therefore converted to a value between 0 and 1. To find the in-focus frame number, the normalized gradient values F_{norm} are plotted as a function of the frame number in the z-stack. The plot is smoothed by interpolating the data points around the maximum of the plot with a fourth-order polynomial. The frame number closest to the maximum of the interpolating polynomial is taken to be the in-focus frame number of the z-stack.

2.2.5. 2D image registration

The image registration employed by our calibration method is concerned with affine transformations such as translation, scaling, and rotation. We assume that there exists, between two different images, an affine transformation

$$\mathfrak{T}: \mathbb{R}^2 \to \mathbb{R}^2, x \longmapsto Ax + d,$$

where $A \in \mathbb{R}^{2\times 2}$ is a square invertible matrix and $d \in \mathbb{R}^{2\times 1}$ is a translation vector. We assume that A can be written as

$$A = cR,$$

where $R \in \mathbb{R}^{2\times 2}$ is a rotation matrix and $c > 0$ is a scale factor. Here R is rigid (i.e., $R^T R = I$) and there is no reflection (i.e., $det(R) = 1$). The translation vector d and rotation matrix R are explicitly given by

$$d = \begin{bmatrix} d_x \\ d_y \end{bmatrix}, R = \begin{bmatrix} cos\,\phi & -sin\,\phi \\ sin\,\phi & cos\,\phi \end{bmatrix},$$

where d_x and d_y are the translations in the x and y directions and $-\pi < \phi \leq \pi$ is the angle of the rotation. To determine the transformation from a source image to a target image, our task is to estimate the parameter vector $\theta = (\phi, d_x, d_y, c)$. Generalized least squares is the correct and optimal statistical procedure for estimating θ [72], as it is unbiased and has minimum variance. For rigid transformations this gives the estimate $\hat{\theta}$ of θ to be

$$\hat{\theta} = (\hat{\phi}, \hat{d}_x, \hat{d}_y, \hat{c}\,) = \arg\min_{\theta} tr(WW^T),$$

where $W = (1 + c)^{-1/2}(t - d1_n^T - cR(\phi)\,s)$, n is the number of source points as well as the number of target points used to determine the transformation, 1_n is an $n \times 1$ vector of ones, $s = \begin{bmatrix} x_{1,src} & \cdots & x_{n,src} \\ y_{1,src} & \cdots & y_{n,src} \end{bmatrix} \in \mathbb{R}^{2\times n}$ is a matrix of the estimated 2D positions $(x_{1,src}, y_{1,src}), (x_{2,src}, y_{2,src}), \dots, (x_{n,src}, y_{n,src})$ of the n points from the source image, and $t = \begin{bmatrix} x_{1,trgt} & \cdots & x_{n,trgt} \\ y_{1,trgt} & \cdots & y_{n,trgt} \end{bmatrix} \in \mathbb{R}^{2\times n}$ is a matrix of the estimated 2D positions $(x_{1,trgt}, y_{1,trgt}), (x_{2,trgt}, y_{2,trgt}), \dots, (x_{n,trgt}, y_{n,trgt})$ of the n points from the target image. In the context of our calibration method, the source and target points are the NanoGrid apertures used for analysis.

2.2.6. Estimation of hole positions

To estimate the axial position of each hole in calibration data set 1 or 2, the in-focus image of the z-stack is first determined as described in Section 2.2.4. From the in-focus image, the imaged holes are detected by a wavelet-based segmentation algorithm [73]. For each detected hole, the region of interest (ROI) is defined as a sub-region centered on the brightest segmented pixel. The ROIs defined in the in-focus image are applied to the other images in the z-stack. To avoid overlap between adjacent ROIs, the ROI size is designed according to the camera pixel size and the distance between two adjacent holes. At the same time, one must also make sure that the ROI size is sufficiently large, such that the images of the NanoGrid holes are well within their confines in every frame of the z-stack. To calculate the axial position of each hole, the same analysis as described in Section 2.2.4 is applied to the ROI corresponding to each hole. However, the z position of the maximum of the interpolating polynomial is taken to be the axial position of the hole in this analysis. Assuming the number of the first frame of the z-stack is set to 1, the z position of a hole is estimated as $z_{pos} = (f_{max} - 1) \times z_{step}$, where f_{max} denotes the frame number of the maximum of the interpolating polynomial and z_{step} is the step size of the piezo nanopositioner or motorized focus drive.

The lateral positions of the holes in calibration data set 1 or 2 are estimated by the least-squares fitting of a 2D Gaussian model [74] to the ROIs in the in-focus image of a z-stack. For calibration data set 3, the lateral positions are determined using all 200 in-focus images of the NanoGrid slide. Here, however, sample drift represents a more prominent effect due to the time required for the sequential acquisition of the 200 repeat images. Therefore, it needs to be corrected for in order to accurately determine the lateral hole positions. To correct for sample drift, the lateral positions of the holes are first estimated from each frame of the data set using the same fitting approach as for calibration data sets 1 and 2. Spatial transformations are then determined between the estimated hole positions for the first image and the corresponding estimated hole positions for the other images using the registration method of Section 2.2.5. The hole positions for each frame are then spatially transformed into the coordinate system of the first frame using the calculated transformation matrices. For each hole, the mean and standard deviation of its 200 spatially transformed coordinates are taken to be its lateral position and localization precision, respectively.

2.2.7. Measurement and adjustment of microscope stage and calibration sample horizontality

The tilt angle of the microscope stage is measured and adjusted as follows. The calibration sample is placed on the microscope stage for 30 minutes before imaging. This is to allow for temperature equilibration between the sample and the microscope to reduce sample drift. Applying the location estimation method of Section 2.2.6 to calibration data set 1 or a z-stack of calibration data set 2, the 3D position of each hole is estimated with high precision. A linear surface model is fitted to the estimated 3D positions using the least-squares criterion. The angle between the fitted plane $z = ax + by + c$ and the horizontal plane $z = 0$ is then calculated using their normal vectors. Furthermore, the difference between the highest and lowest estimated z positions is taken to be the maximum z position difference of the plane in the field of view. Using both the calculated angle and maximum z position difference, the horizontality of the stage is easily adjusted by inserting layers of paper or tape between the mounting frame and the stage at appropriate corners.

The above description, however, requires that the sample itself is flat. Otherwise, this method needs to be adjusted so that the stage is only horizontal if after a 180-degree rotation of the mounting frame with the sample, the measured angle has the same magnitude, but reversed sign.

Using the same approach, the horizontality of the calibration sample is measured and adjusted similarly by attaching layers of paper or tape on the bottom of the slide.

2.2.8. Comparison of data sets

The following analysis is carried out to measure the difference, in terms of the estimates of hole positions, between two calibration data sets acquired of the same NanoGrid sample under different conditions, including the use of different microscopes, different sample orientations, different illumination angles, and different detectors. In this analysis, calibration data set 3 is acquired using each setup and analyzed for comparison. The lateral position of each hole is estimated from each data set as described in Section 2.2.6 and the estimated positions are pair-matched to generate a spatial transformation matrix between the two data sets. For $k = 1, \ldots, K$, where K is the number of pairs of pair-matched holes, denote the kth pair-matched coordinates from the first data set (source data set) as $s_k \in \mathbb{R}^2$and the kth pair-matched coordinates from the second data set (target data set) as $t_k \in \mathbb{R}^2$. Using these pairs of hole positions, the parameters of the affine transformation matrix (i.e., the square invertible matrix $\hat{A}$ and the translation vector $\hat{d}$) are estimated as described in Section 2.2.5. The difference between the kth pair of hole positions is then defined as

$$e_k = t_k - \left[\hat{A}(s_k) + \hat{d}\right], k = 1,\ 2,\ \ldots,\ K.$$

For visualization of the difference pattern, the differences between all K pairs of hole positions are represented with arrows as illustrated in the top panel of Figure 2.1. The arrows in the difference map indicate the difference between each pair of hole positions, in terms of both direction and magnitude. The size of each arrow is chosen to be 200 times larger than the measured magnitude of the difference to allow for a straightforward visual inspection of the difference pattern. In addition, for a representation of the actual differences, the x and y components of the difference between each pair of hole positions are plotted as in the bottom panel of Figure 2.1.

Finally, the root mean squared difference, which we call the “quality score” in this paper, is defined as

$$Q = \left(K^{-1} \sum_{k=1}^{K} \| e_k \|^2 \right)^{\frac{1}{2}},$$

where $\|\cdot\|$ denotes the Euclidean norm on $\mathbb{R}^2$. In some cases, a hole position estimate returned by the fitting of the 2D Gaussian model may be inaccurate. To make sure that these outlying estimates do not bias the score, we use a robust version of the quality score, obtained by excluding the two largest absolute positional differences from the calculation of Q. The quality score represents the overall difference between the two data sets in terms of the deviations between the positional estimates obtained for the NanoGrid holes. If there are significant deviations between corresponding hole positions from the two data sets, the quality score will be high. Conversely, if there are only small deviations between the corresponding hole positions, the quality score will be low.

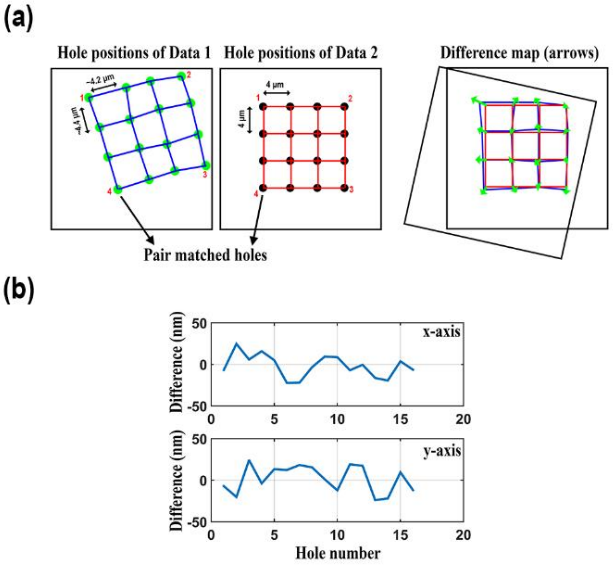

Figure 2.1 Illustration of difference analysis between pairs of hole positions. (a) Visualization of the difference map between two data sets. (b) Line plots of the differences along the x and y axes.

2.2.9. Simulation of calibration data sets

The following simulation is carried out to generate simulated calibration data sets. We first generate 100 points that form a 10 by 10 grid with a uniform spacing of 4 μm between adjacent points (Figure 2.2). Let $s_k \in \mathbb{R}^2$, $k = 1, \dots, 100$, denote the position of the kth grid point. The randomly distorted true position $t_k \in \mathbb{R}^2$ of the kth grid point is then modeled as

$$t_k = s_k + e_k, k = 1, \dots, 100,$$

where $e_k = (e_{k,x}, e_{k,y})$ with $e_{k,x}$ and $e_{k,y}$ the realizations of independent normal random variables with mean 0 and variance α^2. The constant α indicates the overall geometric aberration level.

Subsequently, 200 repeat measurements of each distorted grid point position are generated from a normal distribution. Specifically, for $k = 1, \dots, 100$ and $j = 1, \dots, 200$, the jth repeat measurement $\hat{t}_{k,j}$ of the distorted position t_k is given by

$$\hat{t}_{k,j} = t_k + \epsilon_{k,j},$$

where $\epsilon_{k,j} = (\epsilon_{k,j,x}, \epsilon_{k,j,y})$ represents the measurement error, with $\epsilon_{k,j,x}$ and $\epsilon_{k,j,y}$ the realizations of independent normal random variables with mean 0 and variance σ^2. The constant σ represents the localization uncertainty. The generation of a simulated calibration data set is carried out with a specific choice of the aberration level α and the localization uncertainty σ.

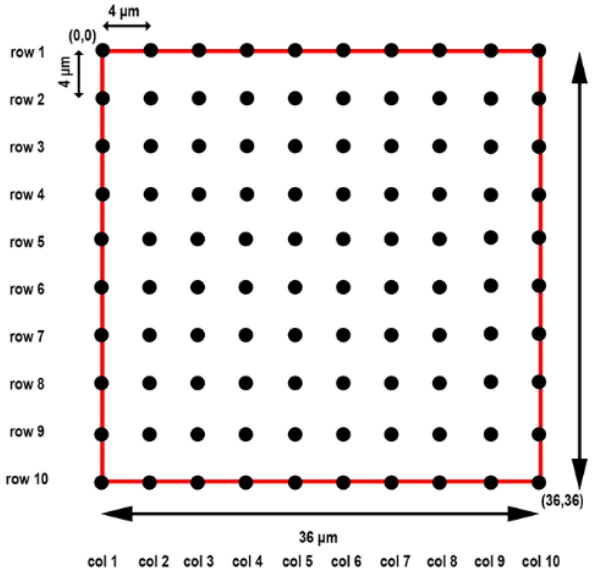

Figure 2.2 Schematic of the simulated 10 by 10 grid points.

2.2.10. Accounting for experimental errors through repeat data acquisitions

Experimental errors intrinsic to the performance of repeat data acquisitions, such as errors associated with the focusing of a sample before each acquisition, places a practical limit on the best (i.e., the lowest) quality score that is attainable for a given microscopy setup. To determine this best quality score for a microscope, the following procedure is carried out. The horizontality of the microscope stage and the calibration sample is first determined and adjusted as described in Section 2.2.7. After acquiring 200 in-focus images of the NanoGrid slide (calibration data set 3), the precise lateral positions of the holes are estimated as described in Section 2.2.6. The sample is shifted along the x- or y-axis, and moved back to its original position. After refocusing, the lateral positions are again estimated after acquiring 200 more in-focus images of the NanoGrid slide. The quality score Q is then determined for the two data sets as described in Section 2.2.8. Importantly, the quality score Q determined for data from such repeat experiments is considered the lowest score Q_{min} that can be experimentally achieved for the given microscope configuration. It is used as a criterion in the determination of reference hole positions (Section 2.2.12).

Note that in the calculation of Q_{min}, the determination of the affine transformation that registers the two sets of lateral hole positions includes the estimation of an angle of rotation, even though the sample is imaged with no change in its orientation after it is returned to its original position. The estimation of the rotation angle is justified, however, by the fact that the repositioning of the sample could potentially introduce a small rotation. Similarly, the estimation of the scale factor is justified by the fact that the refocusing of the sample after repositioning could potentially result in a slightly different magnification. To ensure the validity of the value obtained for Q_{min}, one could always verify that the estimates for the rotation angle and the scale factor are reasonable for the given imaging setup.

2.2.11. Independence of estimated NanoGrid hole positions from the illumination angle

Two sets of 200 in-focus images of the NanoGrid slide (calibration data set 3) are acquired with two different angles of the illuminating light source, namely 0 and 45 degrees. The independence of the estimated hole positions from the illumination angle is then assessed by comparing the two data sets according to the procedure of Section 2.2.8. If the quality score Q is low enough, the estimated hole positions are considered independent from the illumination angle.

2.2.12. Determination of NanoGrid reference hole positions

Reference positions are accurately determined positions of the holes of a NanoGrid calibration sample that are used as a benchmark for comparison with other sets of positional estimates obtained for the same sample. To determine the reference positions, the horizontality of the microscope stage and the calibration sample is first determined and adjusted as described in Section 2.2.7. The precise lateral positions of the NanoGrid holes are then estimated as described in Section 2.2.6 after acquiring 200 in-focus images (calibration data set 3). The sample is rotated 180 degrees. Subsequently, the lateral positions are again estimated after acquiring 200 more in-focus images of the NanoGrid slide. The quality score Q is then determined for these two data sets using the procedure of Section 2.2.8. Whether this microscope is suitable for determining reference hole positions is evaluated using the quality score. If Q is low enough (i.e., close to Q_{min} or some value deemed acceptable for the intended use), the system is considered accurate enough for the determination of reference hole positions, and the hole positions estimated either before or after the 180-degree rotation can be used as reference positions for subsequent calibration analyses.

In addition to the rotation test, it is highly recommended that quality scores are determined for different positions of the NanoGrid slide in the field of view (occupied by the center 10 by 10 holes) to verify the absence of any significant field-dependent aberrations. Specifically, the slide should be positioned at locations that well sample the field of view. In each case, the quality score Q should be calculated with respect to the position at which the rotation test is performed, using the subset of holes that are within the bounds of the field of view for the translated slide position. The value of Q should satisfy a reasonable criterion in all cases in order to consider the system suitable for the determination of reference hole positions. A possible criterion for assessing a given score Q is its closeness to Q_{min} that is calculated with the same subset of holes.

Reference hole positions could alternatively be determined using higher-resolution imaging techniques such as atomic force microscopy and electron microscopy. The approach presented here, however, relies solely on an optical microscope and therefore has the advantage that no additional instrumentation is required.

2.2.13. Evaluation of optical components

2.2.13.1. Axial chromatic aberration analysis for an objective lens

To analyze axial chromatic aberration for an objective lens, calibration data set 2 is acquired with three different color channels whose wavelengths approximately cover the range 400 nm to 700 nm. For example, the three channels commonly employed in fluorescence imaging experiments, namely the FITC, Cy3, and Cy5 channels used in microscope 2 (Section 2.2.2), are suitable choices. The horizontality of the calibration sample and the microscope stage is first determined and adjusted as described in Section 2.2.7. Using a motorized filter cube turret, an image of each of the three color channels is taken per z-step. A z-stack for each color channel, i.e., a total of three z-stacks, is thus acquired. To minimize mechanical drift after each z-step taken by the objective lens or each filter cube turret rotation, the acquisition software waits three seconds before acquiring the image. Given the three z-stacks, the axial positions of the NanoGrid holes are estimated as described in Section 2.2.6 for each channel. The axial hole positions for each channel are averaged, and the distance between the average axial hole positions for a pair of channels is taken to be the axial chromatic aberration between the two channels.

2.2.13.2. Assessment of beam splitter/dichroic filter set performance

The performance of a dichroic filter/dichroic filter set or a beam splitter is assessed by comparing images acquired of its transmitted and reflected light paths. The simultaneous acquisition of the two data sets is carried out using two detectors, as illustrated in Figure 2.3. Specifically, the performance of a dichroic filter/dichroic filter set or beam splitter is analyzed as follows. The horizontality of the calibration sample and the microscope stage is first determined and adjusted as described in Section 2.2.7. After mounting the filter set or beam splitter in the emission image splitter, the precise lateral positions of the NanoGrid holes are independently estimated, as described in Section 2.2.6, from 200 in-focus images of the calibration slide (calibration data set 3) acquired by camera 1 (in the path of the transmitted light) and camera 2 (in the path of the reflected light). The quality score Q is then computed for the two data sets using the procedure of Section 2.2.8. The performance of the dichroic filter/dichroic filter set or beam splitter is then assessed based on the quality score. A low enough value for Q indicates little difference between the images produced by the transmitted and reflected light paths, and the dichroic filter/dichroic filter set or beam splitter is considered to be of high quality. Note that it is important for this analysis that in-focus images are simultaneously acquired by the two cameras. Even though the cameras have been aligned so that they share a focal plane (Section 2.2.2), it is advisable to verify that the in-focus positions for the two cameras, determined by applying the Brenner gradient method separately to z-stacks acquired by the cameras, are in fact the same. This verification should be done before moving the objective lens to the common in-focus position and carrying out the simultaneous acquisition of the 200 images by the two cameras.

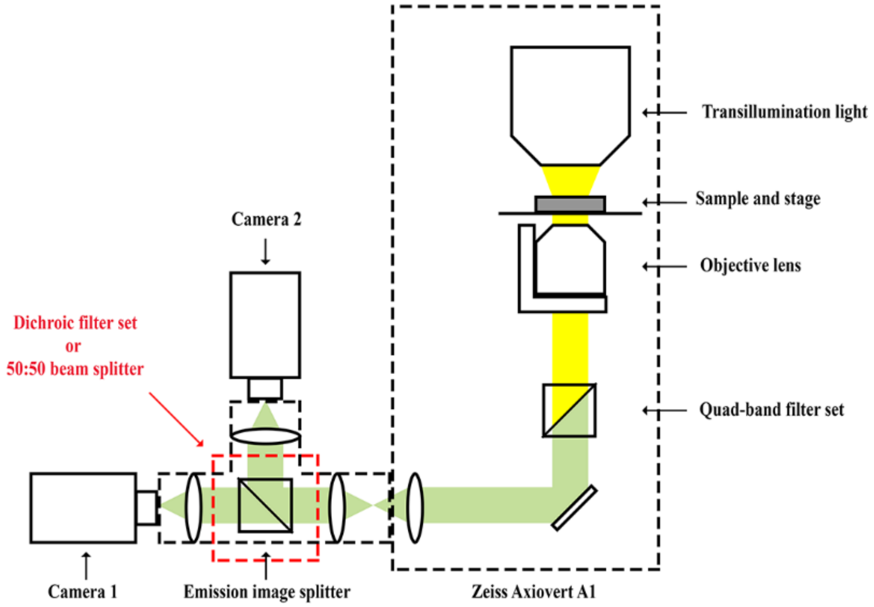

Figure 2.3 Illustration of a microscope setup for dual-color single-molecule imaging.

2.2.14. Software

In the acquisition of data sets for the demonstration of our calibration method, components such as the camera, the piezo nanopositioner, and the filter cube turret were controlled and synchronized using custom software written in the C programming language. The acquired data were processed and analyzed using custom programs written in MATLAB (The Mathworks, Inc) as well as the image analysis software Lumio (Astero Technologies LLC).

2.3. Results

In this section, we demonstrate our calibration method by applying its constituent tools and protocols to specific microscope setups and optical components. Details pertaining to the calibration sample, the instrumentation, the data sets, and the tools and protocols are all as provided in Section 2.2.

2.3.1. Acquisition of z-stack images of a calibration sample

The process of acquiring a z-stack of a NanoGrid sample (Section 2.2.1) is essential for obtaining the three types of calibration data described in Section 2.2.3. Microscope 1 (Section 2.2.2) was used to acquire, in steps of 50 nm, a z-stack of a NanoGrid slide consisting of 50 images (calibration data set 1, Section 2.2.3). In this data set, the center 10 by 10 NanoGrid holes to be used for analysis occupy a field of view of 44.7 µm × 44.7 µm. Since human microvascular endothelial (HMEC-1) cells cultured on coverslips are typically not larger than 45 µm, this cropped field of view is large enough to capture an entire HMEC-1 cell, as shown in Figure 2.4.

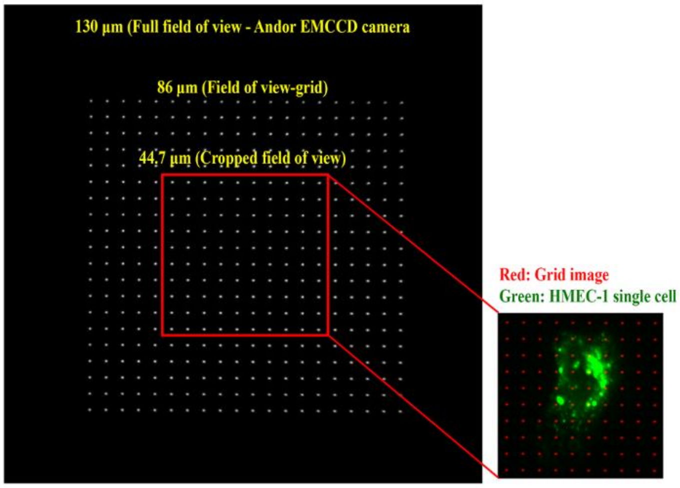

Figure 2.4 Full camera field of view capturing an entire NanoGrid slide. The image shown is the in-focus image from a 50-image z-stack acquired using microscope 1. The red box delineates the cropped field of view that is used for analysis.

2.3.2. Determination of the in-focus image of the sample

Determining an in-focus position is important for precisely estimating the lateral positions of the NanoGrid holes. This is because the closer the image is to focus, the higher the localization precision [75]. The determination of the in-focus image of the z-stack from Section 2.3.1 was carried out using the method based on the Brenner gradient (Section 2.2.4). Figure 2.5a shows the plot of the normalized Brenner gradient versus the z-stack frame number, smoothed by a fourth-order polynomial fitted around the maximum of the plot. Since the frame number closest to the maximum of the interpolating polynomial is 32, the 32nd image of the z-stack, shown in Figure 2.5b, is taken to be the in-focus image of the sample.

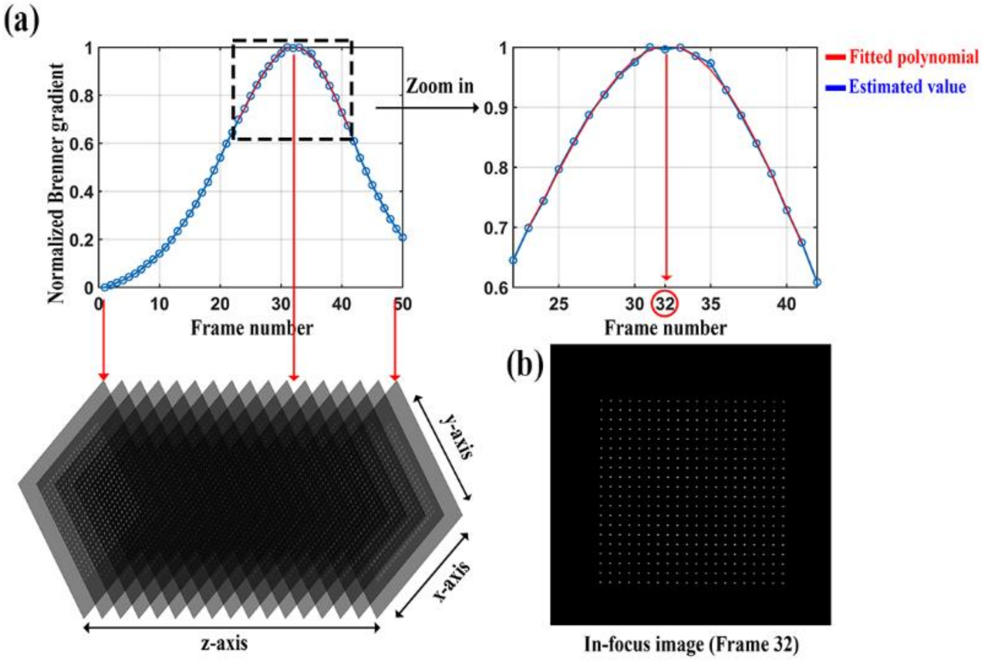

Figure 2.5 Determination of the in-focus image of the sample. (a) A polynomial fit of the normalized Brenner gradient as a function of the z-stack frame number. (b) In-focus image of the sample.

2.3.3. Estimation of lateral hole positions

Our calibration method entails analyses that rely on the precise estimation of the positions of NanoGrid holes. In order to estimate the lateral position of the holes with high precision, we need to acquire a significant number of photons. Therefore, using microscope 1, 200 images of the NanoGrid slide (calibration data set 3) were acquired at the in-focus position determined in Section 2.3.2 with high image brightness. Using the procedure specified in Section 2.2.6, we then estimated the lateral positions of the NanoGrid holes. Due to the time it takes to sequentially acquire 200 images, correction for sample drift represents an important part of the position estimation procedure. Figure 2.6 shows, for a randomly selected hole, the x and y positions estimated from the 200 frames by the fitting of a 2D Gaussian model, before and after drift correction. The standard deviations of the x and y positions before and after drift correction are [1.34 nm, 1.95 nm] and [0.78 nm, 0.64 nm], respectively. This demonstrates that the lateral hole position can be estimated more precisely, by about 41.8% and 67.2% for x and y in this particular case, after drift correction.

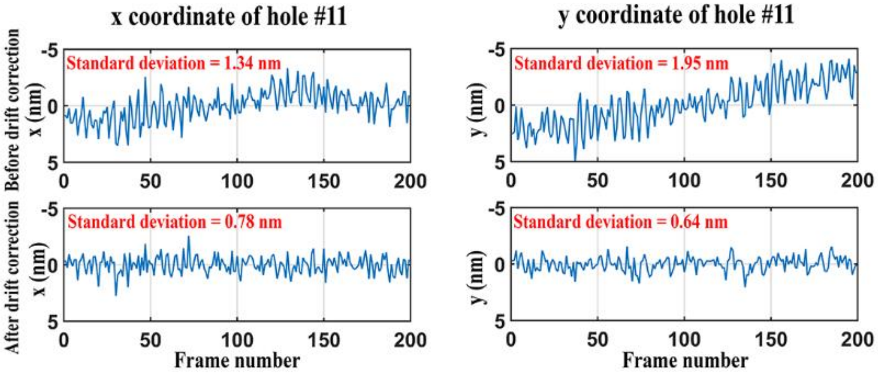

Figure 2.6 Plots showing the estimated x and y positions of an arbitrarily chosen hole over 200 frames, before and after drift correction.

Figure 2.7 shows histograms of the standard deviations of the x and y estimates for all 100 holes. We can see that, for this data set, the localization precision for each hole is less than 1.05 nm and 0.9 nm in the x and y directions, respectively. In addition, the differences between the minimum and maximum standard deviations of the x and y estimates are 0.25 nm and 0.24 nm, respectively, showing that the localization precision is relatively uniform throughout the cropped field of view.

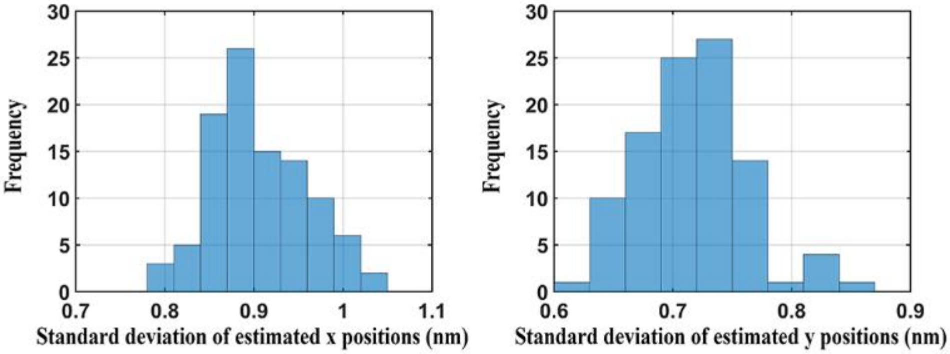

Figure 2.7 Histograms of the standard deviations of the x and y positional estimates for all 100 holes analyzed.

2.3.4. Estimation of axial hole positions

As described in Section 2.2.7 and Section 2.2.13.1, from a calibration data set consisting of one or more z-stacks (i.e., calibration data set 1 or 2), the axial positions of the NanoGrid holes are estimated and used to determine the tilt angle of the stage and sample and the chromatic aberration of an objective lens. To demonstrate the task of estimating axial hole positions, we followed the procedure of Section 2.2.6 and began by extracting as many ROI z-stacks as there are holes from the z-stack data set of Section 2.3.1. This extraction of ROI z-stacks is illustrated in Figure 2.8a. For each hole, the axial position was estimated, as explained in Section 2.2.6, by applying the Brenner gradient-based method for in-focus frame determination to the hole's ROI z-stack. As shown in Figure 2.8b for an arbitrarily chosen hole, since the maximum of the interpolating polynomial from the Brenner gradient-based method occurs at 30.04 frames, the hole's z position is estimated to be 1452 nm, the product of (30.04 – 1) and the piezo nanopositioner step size of 50 nm.

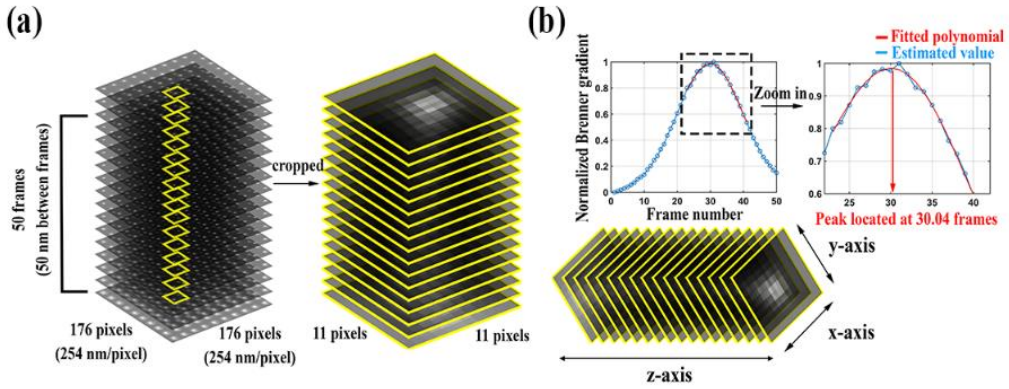

Figure 2.8 Estimation of axial hole positions. (a) An example of an ROI z-stack for a hole. (b) Estimation of the axial position of a hole.

The 3D position of each hole was then given by its estimated z position and its lateral position. As specified in Section 2.2.6, the lateral position was estimated by fitting a Gaussian model to the hole's ROI from the in-focus frame of the z-stack. A wireframe 3D mesh plot showing the 3D positions of all 100 holes is presented in Figure 2.9.

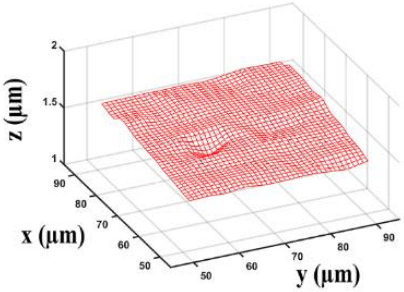

Figure 2.9 A wireframe 3D mesh plot determined by the 3D positions of 100 NanoGrid holes. The blue dots represent the estimated positions of the NanoGrid holes. The wireframe mesh facilitates the visualization of the differences between the z positions of the holes. It is obtained by linearly interpolating the hole positions using a finer grid.

2.3.5. Horizontality adjustment of microscope stage and calibration sample

Wide-field microscopy typically requires the microscope stage to be perpendicular to the optical axis. Therefore, it is necessary to determine the horizontality of the microscope stage and make any needed adjustments. The horizontality of the stage on microscope 1 was measured as described in Section 2.2.7. Figure 2.10a shows, from different viewpoints, the 3D positions of the NanoGrid holes (blue dots) and the fitted plane. The angle between the fitted plane and the horizontal plane and the maximum z difference of the plane in the field of view were determined to be -0.1142˚ and 108.3 nm, respectively. As we could not assume the NanoGrid slide to be flat, we performed the same analysis after a 180-degree rotation of the mounting frame with the sample. The results are shown in Figure 2.10b, and in this case, the angle and the maximum z difference were found to be 0.0702˚ and 66.1 nm, respectively.

(a) Slide in original position

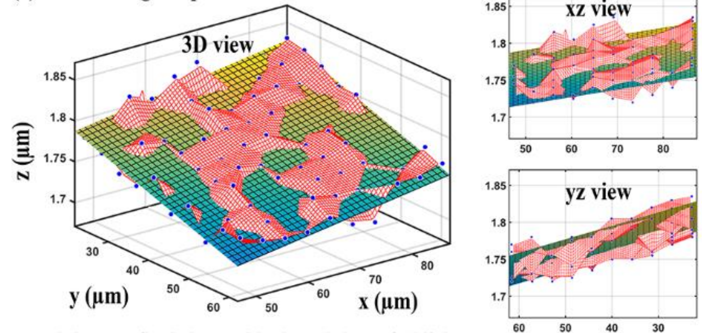

Angle between fitted plane and horizontal plane: -0.1142 degree
Maximum difference between z position estimates: 108.3 nm

(b) Slide in 180-degree-rotated position

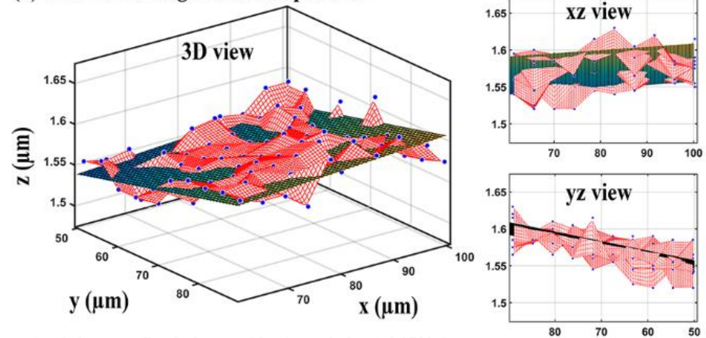

Angle between fitted plane and horizontal plane: 0.0702 degree
Maximum difference between z position estimates: 66.1 nm

Figure 2.10 Estimated 3D positions of 100 holes (blue dots) and the fitted plane before horizontal adjustments when (a) the NanoGrid slide is in its original position and (b) the NanoGrid slide is in its 180-degree-rotated position.

The above results show that while the sign of the tilt angle was reversed after the 180-degree rotation of the mounting frame, the magnitude of the angle had decreased. This indicated that the stage or the sample or both were not horizontal. Therefore, we adjusted the horizontality of the stage and sample as described in Section 2.2.7 and repeated the same analysis. Figure 2.11a shows the results for the data acquired in the original orientation of the sample after adjustment. The angle between the horizontal plane and the plane fitted to the 3D positions of the NanoGrid holes was found to be 0.0257° and the maximum z difference of the plane in the field of view was determined to be 24.3 nm. Figure 2.11b shows that for the data acquired in the 180-degree-rotated orientation of the NanoGrid slide, the angle and the maximum z difference were found to be 0.0088˚ and 8.3 nm, respectively. These results show that, after adjustment, the slopes before and after rotating the sample are similar and close to zero. In other words, both the microscope stage and the calibration sample can now be considered to be horizontal.

(a) Slide in original position

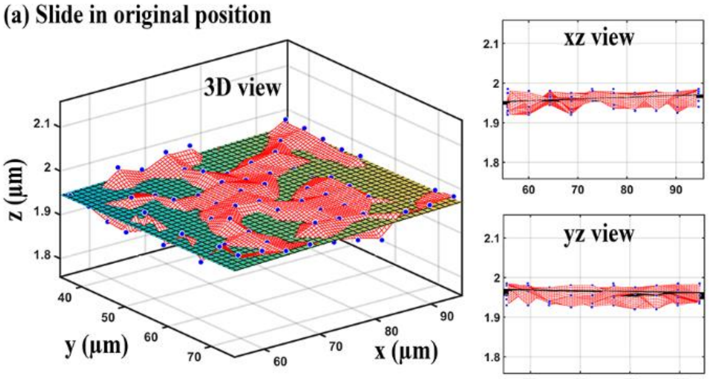

Angle between fitted plane and horizontal plane: 0.0257 degree
Maximum difference between z position estimates: 24.3 nm

(b) Slide in 180-degree-rotated position

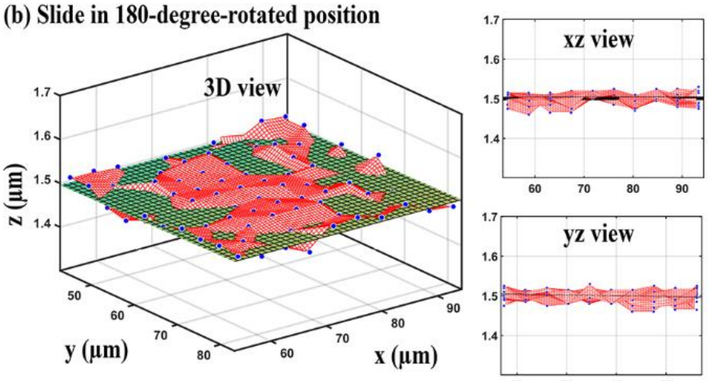

Angle between fitted plane and horizontal plane: 0.0088 degree
Maximum difference between z position estimates: 8.3 nm

Figure 2.11 Estimated 3D positions of 100 holes (blue dots) and the fitted plane after horizontal adjustments when (a) the NanoGrid slide is in its original position and (b) the NanoGrid slide is in its 180-degree-rotated position.

2.3.6. Simulation study investigating the dependence of the quality score Q on the extent of geometric aberration and localization uncertainty

In this section, we investigate the dependence of the quality score Q (see Section 2.2.9) on the uncertainty in repeat measurements of a NanoGrid hole position (i.e., the localization precision) and the overall level of geometric aberration in the microscope system.

We carried out two simulation studies. For the first simulation study (simulation study 1), two calibration data sets were generated as described in Section 2.2.9 for each scenario considered. The scenarios differ in terms of the position measurement uncertainty σ and the level of geometric aberration α, the values of which are given in Table 2.1. For each scenario, the first data set was simulated with no geometric aberrations (i.e., $\alpha = 0$ for the first data set). Geometric aberrations were simulated only in the second data set. Both data sets were generated with the same position measurement uncertainty.

Simulation parameter	Range	Increment
Uncertainty of position measurements σ (nm)	0 – 20	2
Level of geometric aberration α (nm)	0 – 9	1

Table 2.1 Parameter values used for simulation study 1.

Figure 2.12 summarizes the quality score Q for all scenarios considered. The x-axis of the plot represents the overall geometric aberration level α and the y-axis represents the calculated quality score Q. Different colors are used to denote different values of the localization uncertainty σ. We see from the plot that the quality score Q increases with the overall geometric aberration level α. This is as expected, since larger values of α result in larger deviations between the hole positional estimates obtained for the two data sets. The plot also indicates that for a given aberration level α, Q increases with the localization uncertainty σ. In particular, when α is small, comparatively large values of the localization uncertainty can increase the value of Q significantly. Also shown in the plot is the line $y = \sqrt{2}x$. This line is intended as a reference for comparison, since for the data model assumed here, the quality score Q is effectively an estimate of $\sqrt{2}\alpha$ when there is no localization uncertainty (i.e., when $\sigma = 0$) and when one of the data sets is without geometric aberration. Specifically, under these conditions, Q is an estimate of the quantity $\sqrt{Var(X) + Var(Y)} = \sqrt{\alpha^2 + \alpha^2} = \sqrt{2}\alpha$, where X and Y are Gaussian random variables with variance α^2. Indeed, for the data sets analyzed here, we can see that, especially for smaller values of α, Q is relatively close to $\sqrt{2}\alpha$ when σ is small.

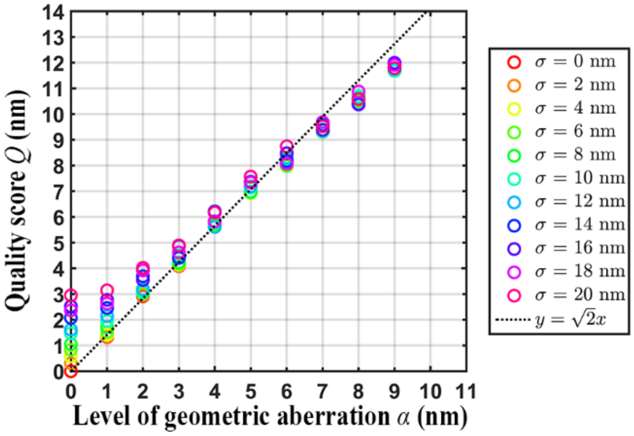

Figure 2.12 Results of simulation study 1, illustrating the dependence of the quality score Q on the level of geometric aberration α and localization uncertainty σ.

The second simulation study (simulation study 2) was carried out the same way as the first study, but with a different range of localization uncertainties. For the second study, the localization uncertainty σ was varied over a more realistic, small-valued range based on what we have observed with our experimental data (see Table 2.2). For the data sets analyzed in this simulation study, we can see that Q is very close to the $\sqrt{2}\alpha$ benchmark for all values of α considered.

Simulation parameter	Range	Increment
Uncertainty of position measurements σ (nm)	0 – 1.4	0.2
Level of geometric aberration α (nm)	0 – 9	1

Table 2.2 Parameter values used for simulation study 2.

Similar to Figure 2.12, Figure 2.13 demonstrates, for simulation study 2, that as the overall geometric aberration level α increases, the quality score Q also increases. However, Figure 2.13 shows that when the localization uncertainty σ is small, it has negligible effect on the value of Q.

The results of our simulation studies indicate that in order to obtain quality scores that accurately reflect the difference in the level of geometric aberration between two data sets, it is important that the NanoGrid hole positions are estimated with high precision (i.e., low localization uncertainty) in both data sets.

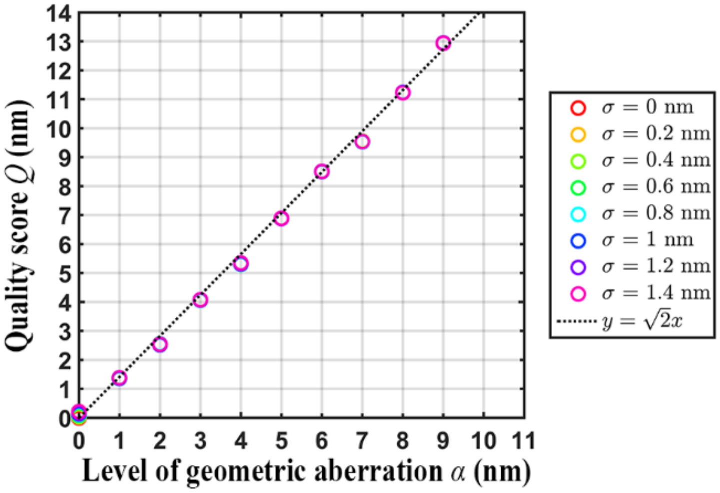

Figure 2.13 Results of simulation study 2, which considers significantly smaller but more realistic localization uncertainties σ than simulation study 1.

2.3.7. Accounting for experimental errors with baseline quality score

To demonstrate the calculation of the baseline quality score Q_{min}, we carried out the analysis procedure described in Section 2.2.10. First, we acquired 200 in-focus images of the NanoGrid slide (i.e., calibration data set 3) using microscope 1. We then moved the sample about 40 μm to the right and then back to its original position. Following this repositioning, we refocused the sample and again acquired 200 in-focus images using the same acquisition settings as before. We then determined the baseline quality score Q_{min} according to the procedure described in Section 2.2.8. Note that the effects of geometric aberration are solely related to the positional coordinates of the NanoGrid holes. For both data sets, since the same sample was imaged in the same position, through Q_{min} we can account for experimental errors that are intrinsic to the acquisition of data, unmingled with the effects of geometric aberration. The left panel of Figure 2.14 shows a plot of arrows indicating the differences between all 100 pairs of corresponding hole positions estimated from the two data sets. The right panel of Figure 2.14 shows plots of the differences in the x and y directions for each pair of corresponding positions. Based on these positional differences, the quality score Q_{min} between the repeat acquisitions was determined to be 1.34 nm. This value is considered the lowest score (i.e., the best score) that can be achieved with the microscope configuration used.

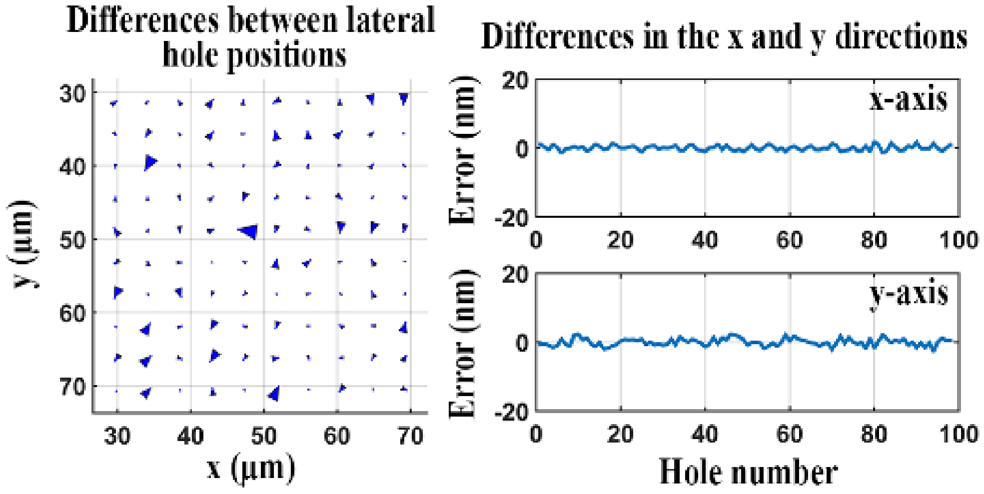

Mean of absolute differences [x, y]: [0.61, 0.89] nm
Median of absoulute differences [x, y]: [0.59, 0.77] nm
SD of absolute differences [x, y]: [0.43, 0.67] nm

Figure 2.14 Difference analysis for data sets acquired before and after repositioning of the NanoGrid slide.

2.3.8. Independence of NanoGrid hole position measurements from the illumination angle

As the NanoGrid slide was illuminated with a LED light source, we wanted to make sure that specifics of the illumination did not impact the results. We therefore imaged the same slide using two different illumination angles of the light source and compared the hole positions estimated from the two data sets.

The procedure followed is as described in Section 2.2.11. In-focus images of the sample were first acquired using microscope 1 with a 0-degree illumination angle (i.e., the illumination light rays traveled parallel to the optical axis and perpendicular to the microscope stage). This was followed by another acquisition of in-focus images of the sample using the same microscope, but with a 45-degree illumination angle. The two data sets were then analyzed as described in Section 2.2.8. The left panel of Figure 2.15 shows a plot of arrows representing differences between the corresponding hole positions estimated from the two data sets. The right panel of the figure shows line plots of the differences in the x and y directions for each pair of corresponding positions.

The quality score Q for the two data sets is 0.96 nm, which is lower than Q_{min} measured in Section 2.3.7. This can be explained by the fact that the second data set here was acquired without first repositioning the sample or the stage. The baseline score Q_{min}, however, accounts for the experimental error that is necessarily introduced when the sample is moved and refocused between acquisitions, and therefore reflects a poorer but more realistic benchmark for what can typically be expected in practice. The result indicates that the overall positional deviation between the two data sets is less than 1 nm, and therefore that the angle of illumination does not impact the measurement of the NanoGrid hole positions.

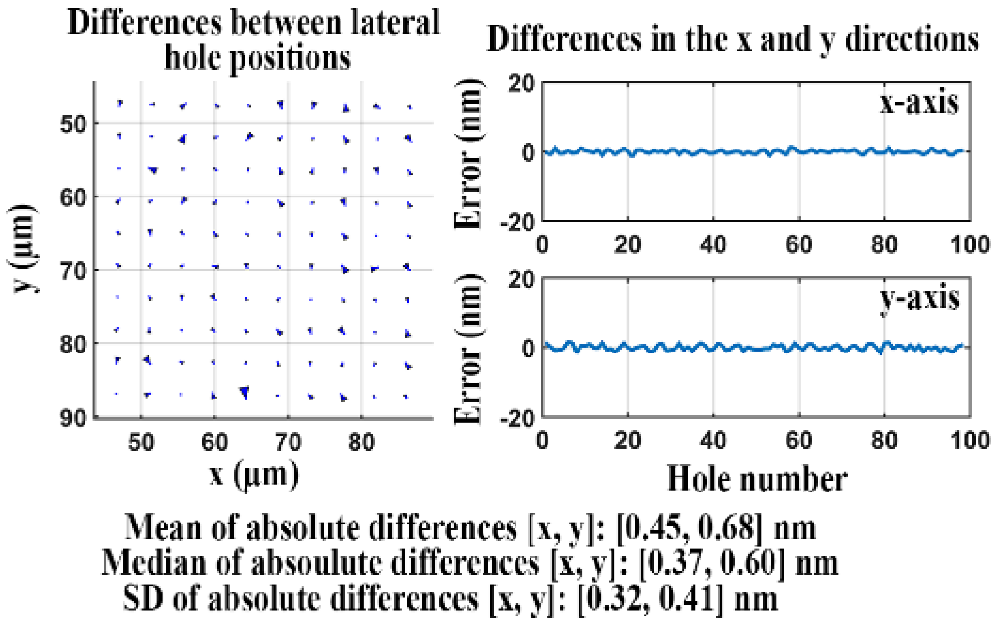

Figure 2.15 Difference analysis for data sets acquired with 0-degree and 45-degree illumination light.

2.3.9. Determination of reference positions of NanoGrid holes

We propose the use of a NanoGrid slide as a calibration standard to evaluate the performance of a microscope system or optical components such as the objective lens and the dichroic filter. The approach is to determine whether the microscope or optical component in question causes geometric aberrations in the light path that are reflected in deviations of hole position estimates from their true positions. As we can expect manufacturing errors in the positions of the NanoGrid holes, we cannot take the holes' nominal positions to be their true positions. Instead, it is necessary for us to determine accurate locations of the holes ourselves, and use them as a reference for comparison. Specifically, we need to be able to very precisely estimate the positions of the holes using a "high-quality" microscope. A high-quality microscope is one that does not introduce significant distortions in the measured hole locations. Therefore, the hole position estimates obtained using such a microscope can be used as reference hole positions for subsequent calibration analyses.

The approach used to establish whether a microscope is suitable for the determination of reference hole positions is as follows. Suppose the calibration sample is imaged before and after a rotation or translation. Any specific pattern associated with the sample should move with the sample, but a geometric aberration pattern should not change with the position or orientation of the sample. This is because geometric aberrations are caused by defects or misalignments in the optics, and not due to variations in the sample. Provided that we use a high-quality microscope, the imaged pattern after the rotation or translation should coincide with the pattern before the rotation or translation. On the other hand, when we use a microscope that distorts the measured locations of the holes, the imaged patterns before and after the rotation or translation will not match well.

Using this concept, the reference positions of the NanoGrid holes were determined as described in Section 2.2.12. Specifically, we acquired 200 in-focus images of the NanoGrid slide (calibration data set 3) using microscope 1, before and after rotation of the sample by 180 degrees. We then compared the two data sets using the procedure of Section 2.2.8. Note that here we omitted the tests described in Section 2.2.12 that involve the translation of the slide to sample different locations of the field of view.

The left panel of Figure 2.16 shows a plot of arrows indicating the differences between the corresponding hole positions estimated from the two data sets, while the right panel shows plots of the x and y components of the differences. The quality score Q for the two data sets is 1.42 nm, which is very close to the baseline score Q_{min} measured in Section 2.3.7. To be precise, it is just 1.06 times larger than Q_{min}. We therefore conclude that microscope 1 is suitable for determining reference hole locations, and we take the estimated positions before rotation of the sample as reference hole positions for evaluations of a microscope system or optical component that utilize the same NanoGrid slide.

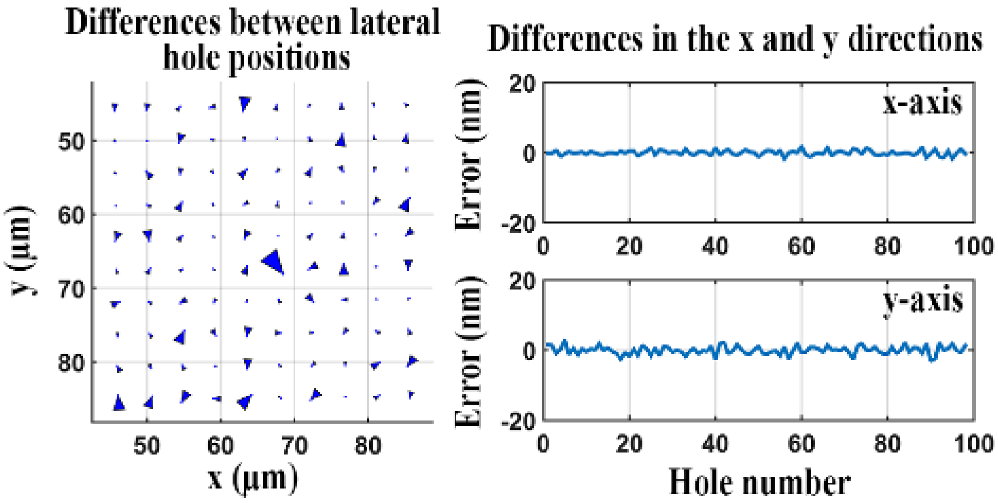

Mean of absolute differences [x, y]: [0.56, 0.98] nm
Median of absoulute differences [x, y]: [0.43, 0.84] nm
SD of absolute differences [x, y]: [0.45, 0.74] nm

Figure 2.16 Difference analysis for data sets acquired before and after slide rotation using microscope 1.

2.3.10. Detection of geometric aberration in the light path

Many microscope imaging systems make use of an objective thread adapter that allows an objective lens to be used on a microscope with a mounting thread that is not of the same pitch or diameter as the objective lens. Such adapters are also often used to increase the axial position of the objective lens. If an inappropriate adapter, such as one that is damaged or one whose thread is incompatible with the thread of the objective lens, is used in a setup, geometric aberrations could be introduced.

To illustrate the analysis of a microscope configuration that exhibits geometric aberration (i.e., a “poor quality” microscope), we installed a damaged thread adapter for use with the objective lens on microscope 1. The evaluation of the microscope system was then carried out as follows, using the reference NanoGrid hole positions determined in Section 2.3.9. The horizontality of the sample and microscope stage was first determined and adjusted using the procedure of Section 2.2.7. We then acquired 200 in-focus images of the NanoGrid slide (calibration data set 3) using this poor quality microscope, and precisely estimated the lateral positions of the NanoGrid holes according to Section 2.2.6. Subsequently, the analysis of the difference between the estimated hole positions and the reference positions was carried out as described in Section 2.2.8.

An arrow plot showing the differences between the estimated hole positions and their corresponding reference positions is provided in the left panel of Figure 2.17. The right panel of the figure shows line plots of the x and y components of the differences. The quality score Q for the two sets of lateral positions is a large 8.67 nm, indicating that the microscope configuration indeed produces significant geometric aberrations.

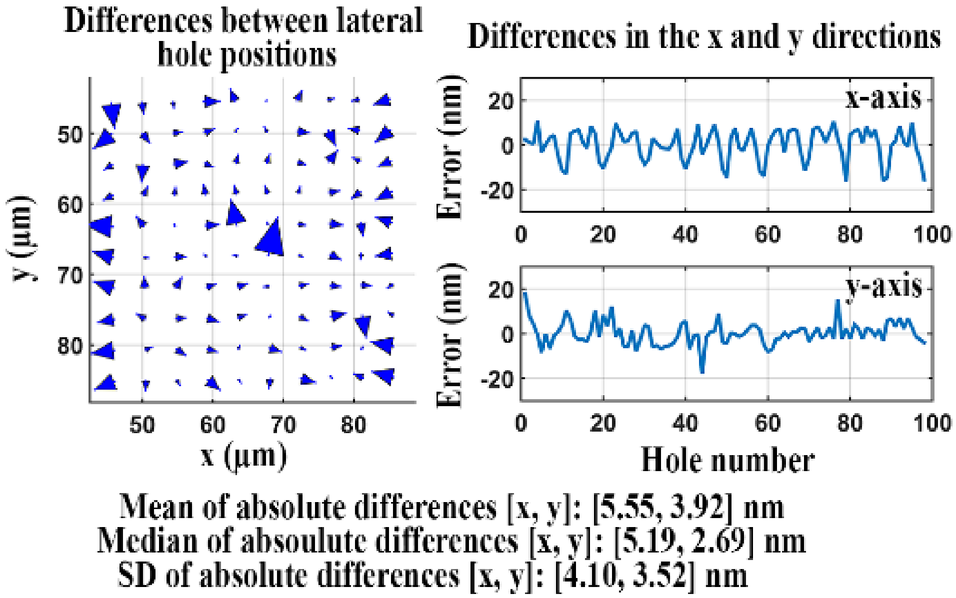

Figure 2.17 Difference analysis for two data sets, one acquired using a reference microscope, the other acquired using an inadequate microscope.

We carried out the same analysis to evaluate a different microscope configuration (microscope 2, Section 2.2.2) and verified that the microscope introduces only a very minor distortion of the hole positions. The much improved results are shown in Figure 2.18, and the quality score Q for the two sets of lateral positions is a significantly smaller 1.76 nm. The small quality score confirms that this microscope configuration introduces only minor geometric aberrations.

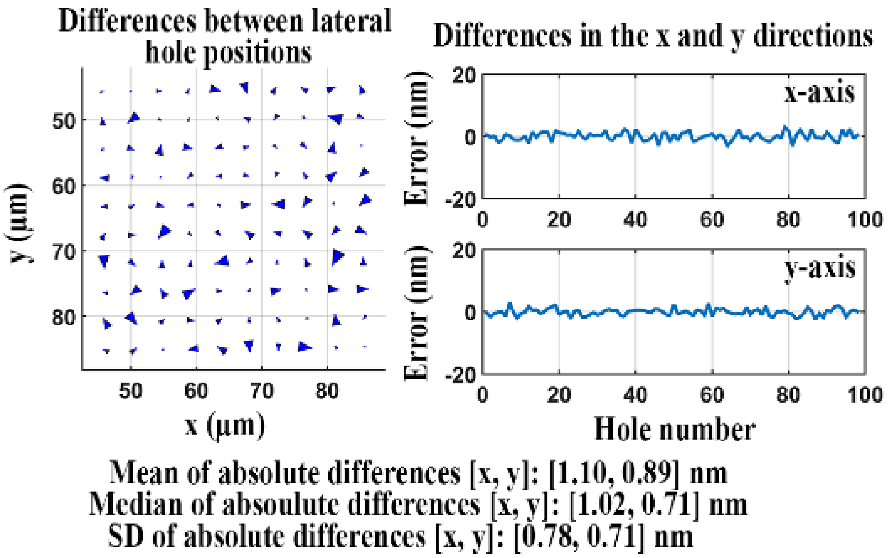

Figure 2.18 Difference analysis for two data sets, one acquired using a reference microscope, the other acquired using a comparable microscope.

2.3.11. Evaluation of optical components

2.3.11.1. Evaluation of axial chromatic aberration of an objective lens

Axial chromatic aberration occurs due to light of different wavelengths refracting differently when propagating through the optical path of a microscope. Even expensive objective lenses may not be fully corrected for wide spectral ranges. It is therefore necessary to analyze an objective lens for axial chromatic aberration. We evaluated the objective lens of microscope 2 using filter sets for three different wavelength ranges, following the procedure detailed in Section 2.2.13.1. The axial and lateral positions of the NanoGrid holes were estimated as described in Section 2.2.6 for each of the three different wavelength ranges considered. Figure 2.19 shows the wireframe mesh plots of the 3D hole positions estimated for the three color channels. The red, green, and blue colors correspond to the results obtained with the FITC, Cy3, and Cy5 filter sets, respectively. The distance between the averages of the axial hole positions for two channels represents the axial chromatic aberration between those channels. As we can see in Figure 2.19, the axial shift between channel 1 (FITC) and channel 2 (Cy3) is 37.89 nm, and the axial shift between channel 2 and channel 3 (Cy5) is 325.54 nm. These results show that the objective lens is not fully corrected when working across a wide spectral range. The aberration is especially severe between the near-infrared range and the blue and green ranges. The axial shift of 37.89 nm between channel 1 and channel 2 cannot be ignored in studies requiring short distance measurements between the two different color probes. The significantly larger axial shift of 325.54 nm between channel 2 and channel 3 could lead to even more serious consequences in any multicolor experimental application. It is therefore important to measure such axial shifts and to take them into consideration when analyzing data acquired in a multicolor experiment.

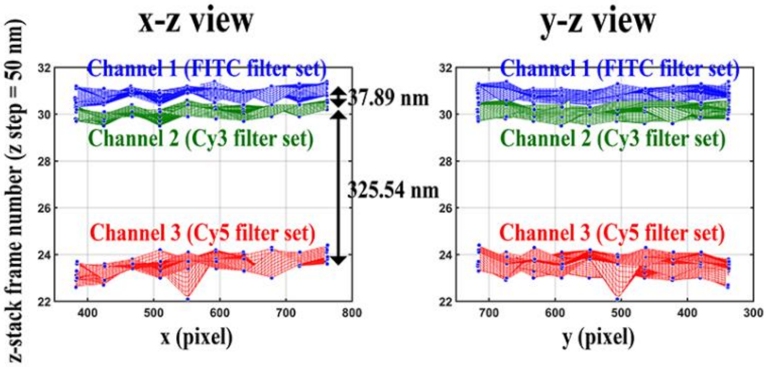

Figure 2.19 Analysis of the axial chromatic aberration introduced by an objective lens.

2.3.11.2. Performance assessment of a dichroic filter set

Cubes pre-mounted with a filter set are available that can be easily integrated into an emission image splitter unit to separate signals of interest by wavelength. A filter set placed in the image splitter typically consists of a dichroic filter and two emission filters.

Unlike conventional microscopy, single-molecule imaging systems are very sensitive to optical wavefront distortions that are potentially caused by a non-flat dichroic filter. The flatness of the dichroic filter has no effect on the light transmitted through the filter, but an insufficiently flat dichroic filter often distorts the wavefront of the light it reflects. Dichroic filters with improved flatness may minimize geometric aberrations in the reflected beam that are obtained with standard dichroic filters. The geometric aberrations caused by a dichroic filter can be detected using the difference between the image transmitted through the filter and the image reflected by the filter. We describe here an application of the approach to dichroic filters of two different types of flatness, standard and improved.

2.3.11.2.1. Standard flatness dichroic filter set

The concept used to determine the quality of a dichroic filter is as follows. Suppose that the calibration sample is imaged with camera 1 in the path of the transmitted emission beam and camera 2 in the path of the reflected emission beam, as shown in Figure 2.3. Provided that the dichroic filter is "perfect", the imaged pattern from camera 2 should match the imaged pattern from camera 1. On the other hand, if an imperfect dichroic filter is used, the imaged pattern from camera 2 will not coincide with the imaged pattern from camera 1 due to distortions introduced by the filter.

Using this concept, the evaluation of the standard flatness dichroic filter set was carried out using microscope 3 as described in Section 2.2.13.2. After mounting the standard flatness dichroic filter set, 200 in-focus images of the NanoGrid slide (calibration data set 3) were separately but simultaneously acquired by camera 1 and camera 2. Two sets of lateral positions were estimated from the two data sets, and the difference between them was analyzed according to Section 2.2.8. Note that by applying the Brenner gradient method of Section 2.2.4 to z-stacks acquired by the two cameras, the cameras' in-focus positions were found to differ by just 0.18 frames, or 9 nm given the z-stack step size of 50 nm. The simultaneous acquisition of the 200 images by the two cameras was therefore carried out at a common in-focus position.

Figure 2.20 illustrates the differences between the lateral hole positions obtained from the data acquired by the two cameras. The quality score Q for the two sets of lateral positions is 6.58 nm, which in this case indicates the overall aberration level in the reflected light path. The relatively large value of Q indicates that this standard flatness filter set is of insufficient quality for nanometer-scale dual color imaging.

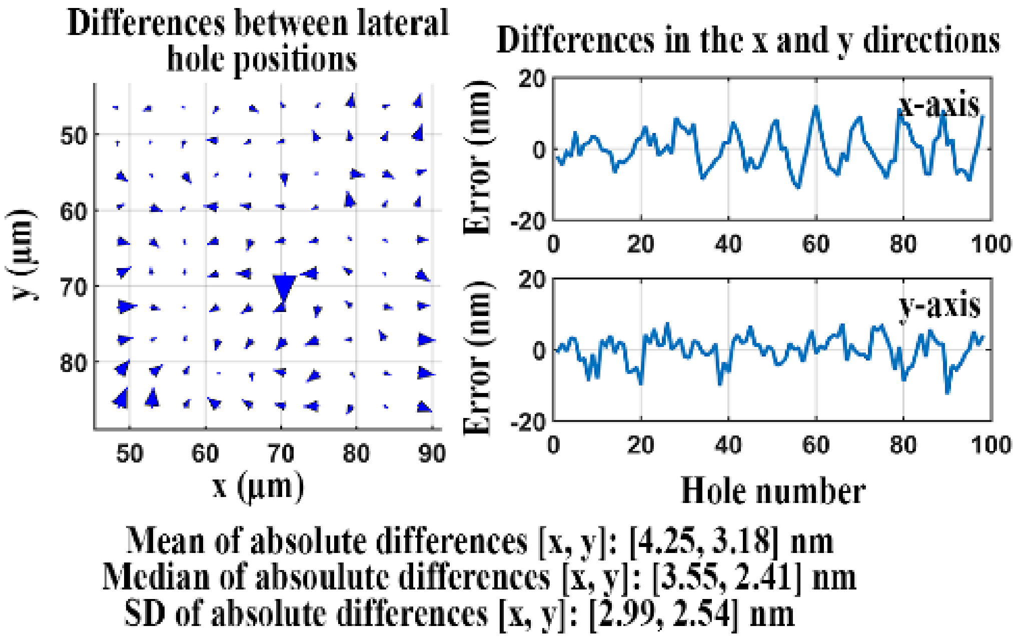

Figure 2.20 Difference analysis for data sets acquired of the transmitted and reflected light paths of a standard flatness dichroic filter.

2.3.11.2.2. Improved flatness dichroic filter set

We carried out the same analysis again using microscope 3, but for a dichroic filter with improved flatness. (In this case, the in-focus positions of the two cameras were also verified to differ by just 9 nm.) The results are shown in Figure 2.21. In this case, the quality score Q for the two sets of estimated lateral hole positions is 2.62 nm. This quality score is significantly smaller than that for the standard flatness dichroic filter, indicating that the improved flatness dichroic filter introduces some distortion in the reflected light path, but to a lesser extent than the standard flatness dichroic filter. Therefore, the improved flatness dichroic filter set should be preferred for experiments that require, for example, nanometer-scale distance measurements between two probes of different colors.

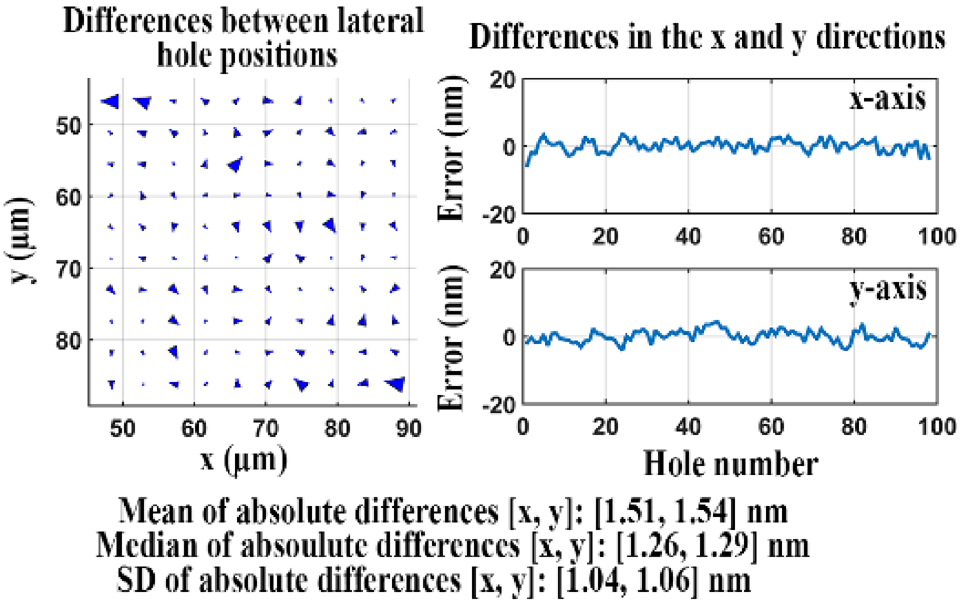

Figure 2.21 Difference analysis for data sets acquired of the transmitted and reflected light paths of an improved flatness dichroic filter.

3. REMOTE-FOCUSING MULTIFOCAL PLANE MICROSCOPY

3.1. Introduction

Studying biological molecules at the single-molecule level is considered to be paramount interest in several fields of inquiry, including subcellular trafficking. Single-molecule fluorescence microscopy is a standard method used in such studies. Studying single-molecule dynamics at the nanoscale requires highly accurate localization of molecules over time. However, the background noise resulting from out-of-focus fluorescence excitation makes it challenging to achieve the desired accuracy. Therefore, to overcome this limitation, selectively illumination of a portion of the sample, such as total internal reflection fluorescence [76,77] and highly inclined and laminated optical sheet [78] microscopy, has been widely used to study the dynamics of individual molecules. However, the majority of significant biological events are inherently 3D fast dynamic processes, which pose significant challenges for imaging their subcellular trafficking using conventional fluorescence microscopy.

Therefore, various 3D single-molecule tracking techniques have been introduced in several studies [34,37,51]. In particular, MUM allows simultaneous imaging of widely spaced focus levels and monitoring of fast-moving single molecules with cellular structures [37]. In this configuration, as the number of focal planes increases, the number of photons detected by each camera decreases, making it harder to perform an accurate 3D reconstruction of small intracellular organelles, such as endosomes and lysosomes, in which individual molecules of interest interact. Hence, to overcome this limitation, our laboratory has demonstrated a new 3D imaging modality called rMUM [48,49]. This imaging system consists of two imaging modules: a MUM-module and a remote-focusing module (r-module). The MUM-module images the trajectories of single molecules in 3D, whereas the r-module performs 3D volumetric imaging of the cellular context. Volumetric contextual imaging is achieved by sequentially scanning the specimen along the optical axis without having to physically move the specimen.

Generally, rMUM is a complex imaging system that consists of several optical compartments and mechanical devices and generates a complex array of microscopy image datasets. Such an intricate and sophisticated system warrants detailed calibration protocols and data analysis to perform meaningful biological studies at the nanoscale level.

Therefore, in this section, we describe a calibration protocol for assessing the performance of a microscope, including 3D localization accuracy and spatial registration error between two different color channels, to address the various points raised above. This approach is based on imaging a lithographically fabricated aperture array and analysis algorithms, such as the estimation of the 3D position of imaged apertures, spatial registration, and focal shift correction between two different color channels.

3.2. Calibration protocol

3.2.1. Microscope setup

Generally, an rMUM setup comprises an excitation module, a standard microscope, and two emission modules: a MUM-module and an r-module. To perform calibration, a commercially available standard NanoGrid slide (Miraloma Tech, LLC) is trans-illuminated with an LED (M810L3-C4; Thorlabs). An illustration of the light path of the rMUM setup is shown below in Figure 3.1. In live-cell imaging, the specimen is illuminated with two different lasers: a 488 nm diode laser (Toptica) and a 635nm diode laser (OptoEngine). Then, the excitation light is filtered using a quad-band dichroic filter (Di01-R405/488/561/635-25x36; Semrock) before illuminating the specimen. The light emitted from the specimen is first captured by a 63×/1.4 numerical aperture (NA) Zeiss Plan-Apochromat objective lens (O1) and then filtered by a quad-band emission filter (FF01-446/523/600/677-25; Semrock). Then, the light is separated into two light paths by a dichroic filter set (FF01-731/137-25; Semrock). The light reflected by the dichroic filter set is directed toward the MUM-module that is implemented with three 50:50 beam splitters (21014; Chroma), which further split the light into four identical EMCCD cameras (iXon DU897-BV; Andor). These cameras are used in conventional readout mode. Each camera is placed at a certain distance from the tube lens of the microscope and configured such that the inter plane distances are 1.21, 1.24, and 1.27 µm. Then, the light transmitted through the dichroic filter set is directed toward the r-module, which consists of two identical objective lenses 40×/0.95 NA Zeiss Plan-Apochromat. These objective lenses (O2, O3) are placed against each other, with the first lens facing the camera and the other one facing the microscope’s body. The first objective lens projects a replica of the specimen onto an intermediate focal plane, and the second objective lens projects a magnified image of the replica onto an sCMOS camera (Zyla 4.2; Andor). The second objective lens is mounted on a piezo nanopositioner which moves it along the optical axis to image different focal planes within the specimen's replica. The cameras are used in conventional readout mode. All components, including the cameras, lasers, shutters, and piezo nanopositioners, are controlled and synchronized using software that is custom-written in C programming language. All the acquired data are processed and analyzed as detailed in the next sections.

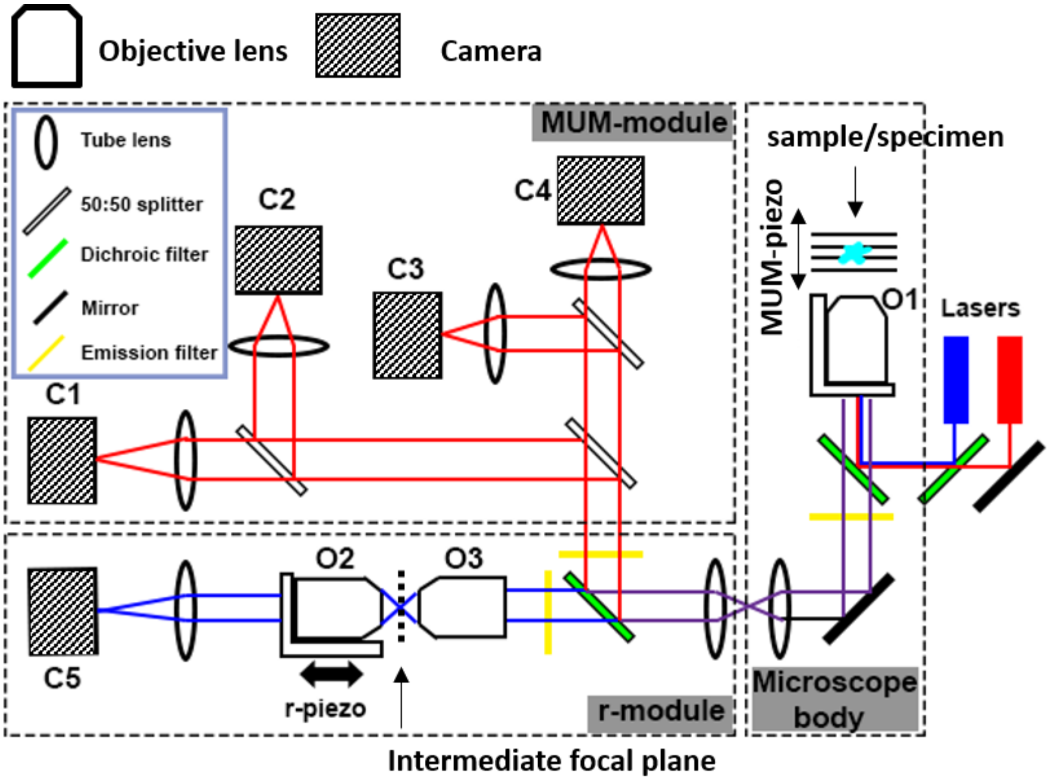

Figure 3.1 Illustration of the light path of the rMUM setup.

3.2.2. Acquisition of calibration data

Highly accurate calibration data are essential to obtain reliable experimental data. Calibration data sets are acquired as follows. First, a NanoGrid sample is placed on a primary imaging objective lens and left undisturbed for 10-min to avoid thermal drift before imaging. The sample is then moved along the optical axis using a MUM-piezo nanopositioner in increments of 200 nm, over a total depth of 10 µm. A total of 25 images are acquired for every increment by four cameras in a MUM-module, resulting in four sets of z-stack images. At each level of the piezo nanopositioner, a z-stack of the NanoGrid is acquired by an sCMOS camera of an r-module. Then, z-stack acquisition in the r-module is achieved by moving the r-piezo nanopositioner in increments of 300 nm, over a total depth of 14.7 µm, wherein a single image is acquired for every increment (Figure 3.2).

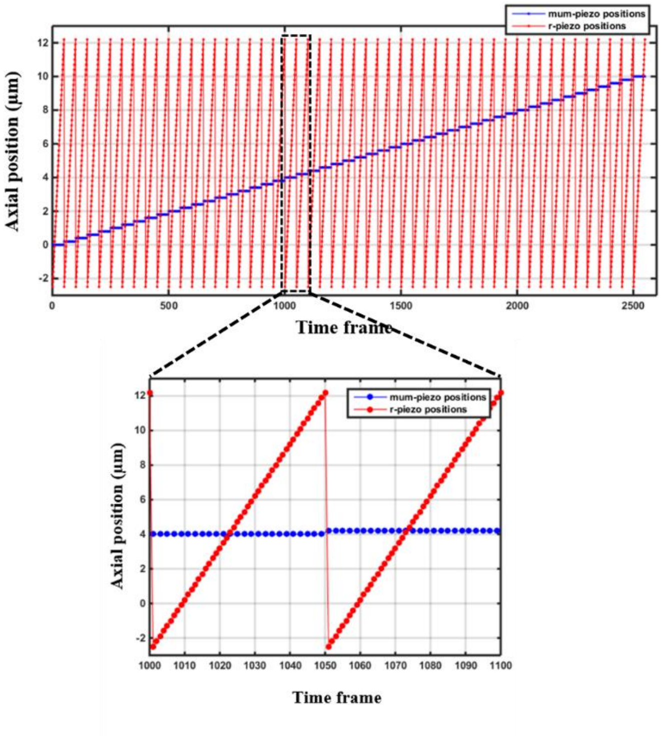

Figure 3.2 Illustration of the acquisition of calibration datasets. The upper plot shows the axial positions of both the MUM- and r-piezo nanopositioners at each acquisition frame. The r-module acquires images two times faster than the MUM-module. The bottom plot shows a zoomed-in region of a small window in the upper plot (shown as a black dashed box).

3.2.3. Arrangement of calibration data

The calibration data set in Section 3.2.2 is arranged in a multistep process, as shown in Figure 3.3. The acquired calibration data set (“ImageSet1”) consists of all the images acquired by the four MUM-module cameras (C1-C4) as well as all the images acquired by the r-module camera (C5). First, two image sets called 'MUM-sorted' and 'r-sorted' are created from the initial ImageSet1.The first set contains all the MUM-images, and the second set contains all the r-images. The MUM-sorted image set is arranged such that one can view four independent z-stacks images taken at a 200 nm increment by displacing the main objective lens over a depth of 10 μm, for how many ever repeat as mentioned while acquiring. On the other hand, the r-sorted image set is arranged such that one can view an entire z-stack of relay scans taken at a 300 nm increment over a depth of 14.7 μm for every 200 nm axial displacement of the sample (using main objective piezo motion). This type of data arrangement allows the user to visualize images effectively and aids in the data analysis of experimental data sets.

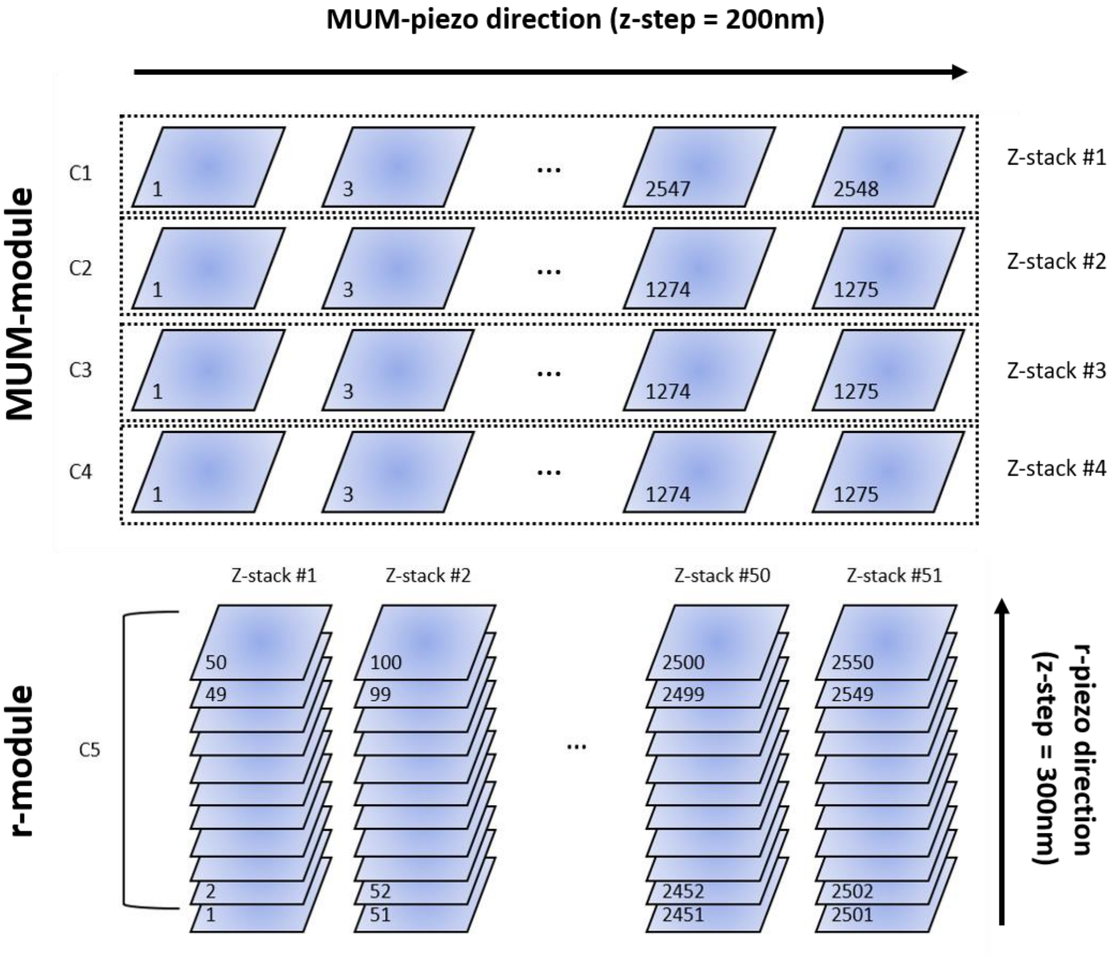

Figure 3.3 Illustration of the arranged datasets. The upper panel shows the 'MUM-sorted' data set and the bottom panel shows the ‘r-sorted’ data set. The acquired images are represented as rectangles, and the number in each image indicates the acquisition frame number (Figure 3.2).

3.2.4. Focal shift correction for the r-module

In the rMUM configuration, we used objective lenses with distinct properties in the r-module and MUM-module. For example, the MUM-module uses an oil immersion objective lens with a magnification of 63× and an NA of 1.4, whereas the r-module uses two identical air objective lenses with a magnification of 40× and an NA of 0.95. If we assume that the two objective lenses in the r-module have the same magnification and that all of the tube lenses used in the rMUM setup have the same focal length, then the total lateral magnification of the image obtained by camera C5 in the r-module is given by the following formula [79]:

$$M_{total} = M_1 \times \frac{n_2}{n_1},$$

where M_1 denotes the lateral magnification of MUM-objective lenses (O1) and n_1 and n_2 denote the refractive indices of immersion media corresponding to the MUM-objective lens (O1) and r-objective lenses (O2, O3). The theoretically calculated lateral magnification (M_{total}) of our rMUM configuration is 41.5 ($M_1 = 63$, $n_1 = 1$, and $n_2 = 1.5$).

However, because of the differences in the immersion media between the MUM-objective lens and the r-objective lenses, displacement of the r-piezo nanopositioner along the optical axis often results in a displacement of the focal plane of a different magnitude. This phenomenon is generally known as “focal shift” and is typically corrected by multiplying n_1/n_2 by the displacement of the focal plane [80]. It should be noted that theoretical calculations are often not accurate when applied to practical settings. For example, during the acquisition of calibration data, when the r-piezo is moved in increments of 300 nm for the axial scanning of the sample, the focal plane is moved in increments that are less than the predicted value ($300\,nm \times n_1/n_2 = 300\,nm\ \times 1/1.515 = 198$ nm). If not accounted for, this step size mismatch may negatively impact the accuracy of the 3D reconstruction of the data collected by the r-module. In order to correct this mismatch, we propose an approach for determining the factor that converts between the r-piezo nanopositioner and focal plane displacement.

This approach is outlined as follows. In the MUM-module, a z-stack is acquired by moving the MUM-piezo 50 steps in increments of 200 nm, as described in Section 3.3.2. As there are four focal planes and one detector per focal plane, four such z-stacks are acquired by the MUM-module. For each z-stack, the index of the frame that contains the in-focus image of the sample is determined as described in Section 2.2.3. Let $\mathrm{I}_{\mathrm{p1}}^{\mathrm{MUM}}, \mathrm{I}_{\mathrm{p2}}^{\mathrm{MUM}}, \mathrm{I}_{\mathrm{p3}}^{\mathrm{MUM}}$, and $\mathrm{I}_{\mathrm{p4}}^{\mathrm{MUM}}$ denote the in-focus frame indices of the first, second, third, and fourth focal planes, respectively, of the MUM-module. In the r-module, for each MUM-piezo step, a z-stack is acquired by moving the r-piezo 51 steps in increments of 300 nm, as described in Section 3.2.2. The r-module, therefore, acquires a total of 50 z-stacks. The in-focus frame index of each z-stack is determined in the same way as for a MUM-module z-stack.

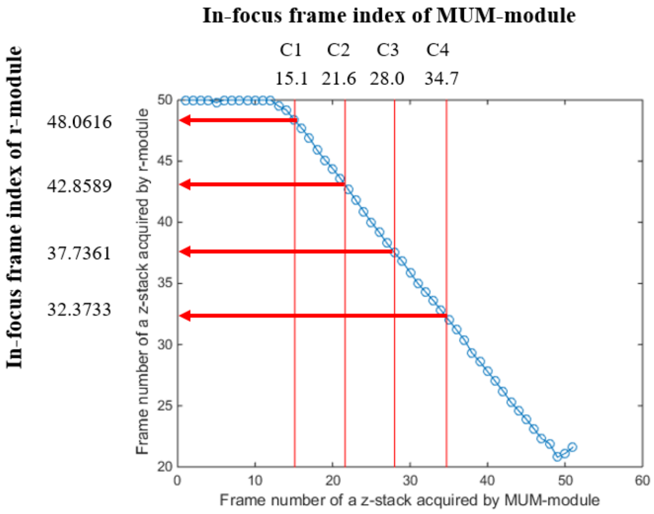

Figure 3.4 Determination of in-focus frame indices of MUM- and r-module.

In Figure 3.4, the x- and y-axes represent the frame indices of a z-stack acquired by the MUM-module and r-module, respectively. The red lines indicate the in-focus frame indices for the z-stacks acquired by the MUM-module, whereas the blue circles indicate the in-focus frame indices for the z-stacks obtained by the r-module at each MUM-piezo step.

When the sample comes into focus with respect to each MUM-module cameras, the in-focus frame index of a hypothetical r-module z-stack is determined as follows. A piecewise linear function is fit into the in-focus frame indices for the 50 acquired r-module z-stacks (i.e., the blue circles in Figure 3.4). The in-focus frame index of a hypothetical r-module z-stack corresponding to an in-focus position of the MUM-module is then obtained as the value of this piecewise linear function at the frame index for the MUM-module in-focus position. With this interpolation approach, when the sample comes into focus with respect to the four MUM-module cameras, the in-focus frame indices for the four hypothetical r-module z-stacks are determined as the value of the piecewise linear function at the four in-focus frame indices for the MUM-module (i.e., at $\left[\mathrm{I}_{\mathrm{p1}}^{\mathrm{MUM}}, \mathrm{I}_{\mathrm{p2}}^{\mathrm{MUM}}, \mathrm{I}_{\mathrm{p3}}^{\mathrm{MUM}}, \mathrm{I}_{\mathrm{p4}}^{\mathrm{MUM}}\right]$ = [34.7, 28.0, 21.6, 15.1]). For the example shown in Figure 3.4, this method yields in-focus frame indices of 32.3733, 37.7361, 42.8589, and 48.0616 for the hypothetical r-module z-stacks corresponding to the in-focus frame indices of the first, second, third, and fourth focal planes, respectively, of the MUM-module. We denote these indices by $\mathrm{I}_{\mathrm{p1}}^{\mathrm{r}}, \mathrm{I}_{\mathrm{p2}}^{\mathrm{r}}, \mathrm{I}_{\mathrm{p3}}^{\mathrm{r}}$, and $\mathrm{I}_{\mathrm{p4}}^{\mathrm{r}}$, respectively.

Using the first and second focal plane positions of the MUM module, the focal plane displacement s_{fp12}^{r} in the r-module, corresponding to the r-piezo step size $\mathrm{s}_{\mathrm{piezo}}^{\mathrm{r}}$ = 300 nm, is then given by

$$s_{fp12}^{r} = \frac{(I_{p1}^{MUM} - I_{p2}^{MUM}) \times s_{piezo}^{MUM}}{(I_{p1}^{r} - I_{p2}^{r})}$$

where $\mathrm{s}_{\mathrm{piezo}}^{\mathrm{MUM}}$ = 200 nm denotes the MUM-piezo step size. We assume that the MUM-piezo step size is the same as the corresponding focal plane displacement ($\mathrm{s}_{fp}^{\mathrm{MUM}}$) in the MUM-module. The same calculation is also performed using the other pairs of adjacent focal plane positions (i.e., the second and third focal plane positions, as well as the third and fourth focal plane positions). The final focal plane displacement ($\mathrm{s}_{\mathrm{fp}}^{\mathrm{r}}$) is then determined by averaging the three values. To convert between r-piezo displacement and focal plane displacement, the factor α is given as follows:

$$\alpha = \frac{s_{fp}^{r}}{s_{piezo}^{r}}.$$

From the calibration data acquired in Section 3.2.2, the conversion factor α is 0.5337.

3.3. Performance evaluation of rMUM

3.3.1. Spatial registration accuracy

Our microscope system consists of two different modules that generate 3D single-molecule trajectories and contextual data simultaneously using five different cameras. In our experiments, two different proteins in cells were tagged with different fluorophores and imaged using two different coordinate systems (i.e., Qdot 705 for the MUM-module and GFP for the r-module). To analyze these images, the two different coordinate systems need to be spatially registered into one coordinate system with a high level of accuracy. In the case of the MUM-module, four identical cameras are used to image four distinct focal planes simultaneously. To facilitate data mining and 3D localization using the image data sets, we need to spatially transform the coordinate systems of the four different cameras into one reference coordinate system.

Spatial registration is performed as follows. The calibration data set is first acquired, as described in Section 3.2.2. For example, in the case of the MUM-module, a z-stack acquired from each camera is generated by moving the MUM-piezo nanopositioner in increments of 200 nm (i.e., a total of four z-stacks). For the r-module, when the sample comes into focus with respect to the first MUM-module camera, a z-stack is acquired by moving the r-piezo nanopositioner in increments of 300 nm. The in-focus images from each z-stack are determined by the in-focus frame index calculated as described in Section 2.2.4.

The imaged holes are detected using a wavelet-based segmentation algorithm [73]. The region of interest (ROI) is defined as a subregion around the brightest segmented pixel for each imaged hole. Lateral hole positions are estimated by least-squares fitting of a 2D Gaussian model [21] to the ROIs containing a hole in the in-focus image of a z-stack.

Let the n^{th}-pair-matched estimated hole positions in the coordinate system of Cameras 1 and 2 denote (x_n^{c1}, y_n^{c1}) and (x_n^{c2}, y_n^{c2}), $n = 1, \ldots, N$, where N is the number of pairs of pair-matched holes. The coordinate system of Camera 1 here is set as a reference coordinate system. Spatial transformations are determined between pair-matched holes on the basis of the generalized-least squares criterion [81]. Subsequently, the hole positions in the coordinate system of Camera 2 are spatially transformed into the reference coordinate system of the holes using the calculated transformation matrices. Let the n^{th} - spatially transformed hole positions in the coordinate system of camera 2 denote $(\hat{x}_n^{c2}, \hat{y}_n^{c2})$. The registration error between pair-matched holes after registration is then determined by computing the root mean square (RMS) of the differences between (x_n^{c1}, y_n^{c1}) and $(\hat{x}_n^{c2}, \hat{y}_n^{c2})$, n = 1, …, N. The same process is performed between the reference coordinate system and the other coordinate systems to generate transformation matrices (i.e., the coordinate system of Cameras 1 and 3, the coordinate system of Cameras 1 and 4, and the coordinate system of Cameras 1 and 5). Figure 3.5 shows the results for the image registration.

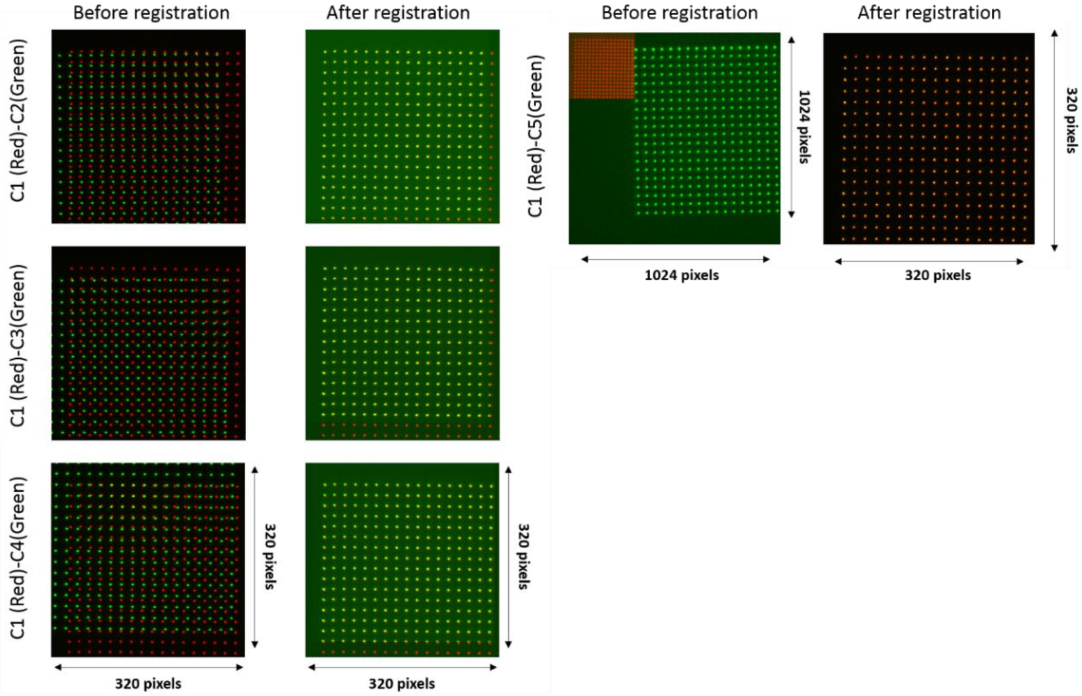

Figure 3.5 Overlay of the calibration images before and after image registration.

In Figure 3.6, the differences between the hole positions estimated in the reference coordinate system and the hole positions spatially transformed from the other coordinate systems are shown as histograms. The RMS values of the differences (i.e., registration error) for the x and y axes are [1.6292 nm, 2.8484 nm], [1.8989 nm, 2.7626 nm], [2.8430 nm, 4.1451 nm], and [6.4313 nm, 5.2216 nm].

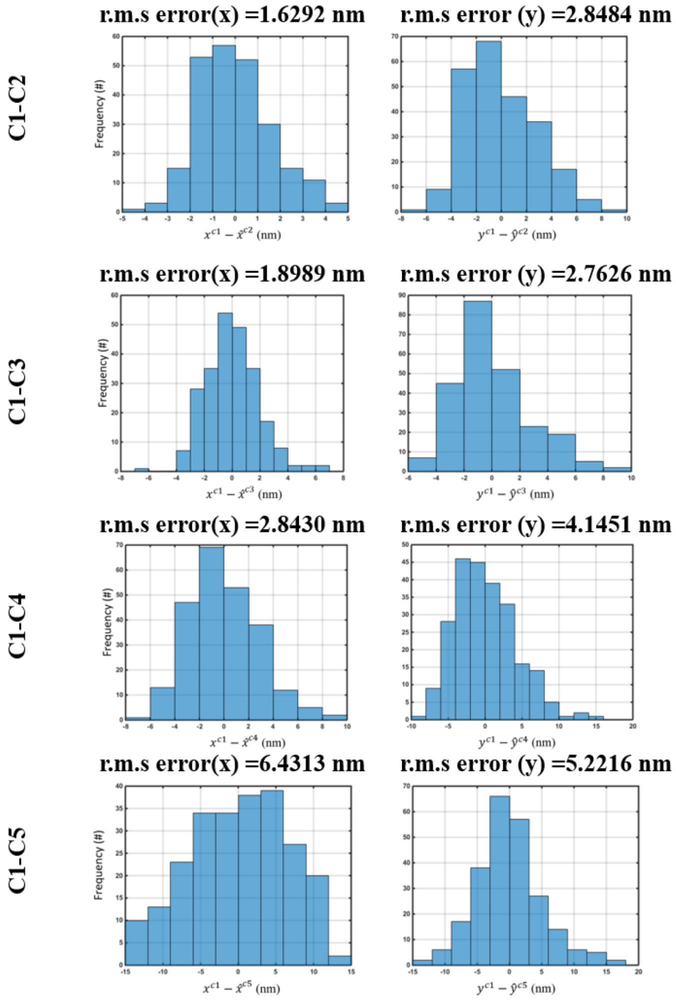
r.m.s error(x) =1.6292 nm
r.m.s error (y) =2.8484 nm
r.m.s error(x) =1.8989 nm
r.m.s error (y) =2.7626 nm
r.m.s error(x) =2.8430 nm
r.m.s error (y) =4.1451 nm
r.m.s error(x) =6.4313 nm
r.m.s error (y) =5.2216 nm

Figure 3.6 Histograms of the registration errors in the x and y axes.

3.3.2. 3D single-molecule localization accuracy

In general, 3D single-molecule localization microscopy relies on fitting the images of individual molecules with an analytical model that approximates the PSF of the microscope [82,83]. Traditionally, the implementation of this technique has been hindered by the issue of finding an analytical model that reasonably describes the PSF (i.e., one that adequately matches the image of a single molecule). For example, analytical models do not typically account for optical aberrations due to imperfections in the lens and misalignment of the optical elements in the microscope's light path. Furthermore, it is often difficult to determine the precise values of the imaging system parameters required by an analytical model. To overcome these problems, we adopted an approach that, instead of an analytical model, uses a model that is determined by the interpolation of an experimentally collected set of images with a smoothing spline [84–86].

In our approach, the image of a point source (i.e., PSF) is represented in 3D by a z-stack (i.e., a stack of images acquired at different levels of defocus). In the case of the MUM-module, the PSF representation is therefore obtained by simultaneously acquiring four z-stacks of NanoGrid with respect to four distinct focal planes (Section 3.2.2) and cropping out the images of an arbitrary hole. The center of the selected hole, typically the brightest pixel, should be in the center of the cropped area. To avoid overlapping with the image of an adjacent hole, we set the crop size on the basis of some factors, such as the camera's pixel size, the magnification of the microscope's optics, and the distance between two adjacent holes. Each z-stack of the isolated hole, which provides a discrete 3D representation of the PSF, is then interpolated with a 3D B-spline to produce a continuous representation of the PSF (Figure 3.7). The interpolation is then performed with a specific choice of the smoothing factor γ, the derivative order l, and the B-spline degree d [84–86].

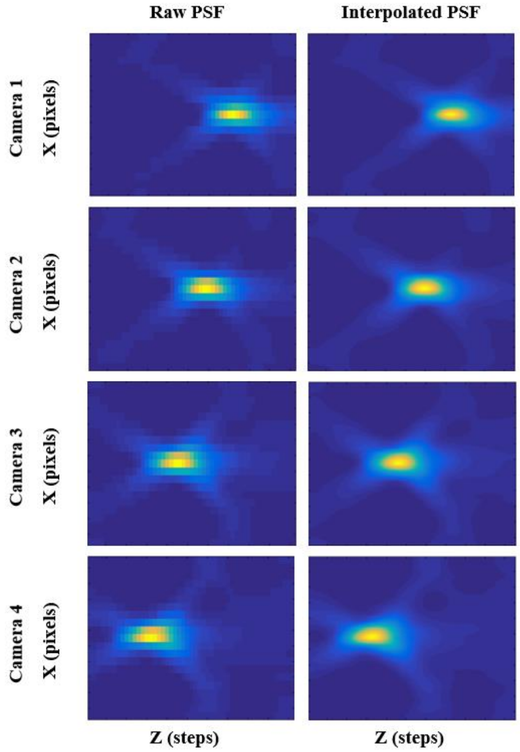

Figure 3.7 Comparison of PSFs. The figure shows the yz-projection of experimentally collected PSFs and interpolated PSFs from C1, C2, C3, and C4 (from top to bottom). The average percentage errors between raw and interpolated PSFs for each camera are 1.27%, 1.58%, 1.42%, and 1.74%, respectively.

In this study, we use an analytical approach called MUMLA [37] to estimate the location of individual molecules from data acquired simultaneously at different focal planes. We assume that a pixelated detector $\left\{C_1, \ldots, C_{K_{pix}}\right\}$ obtains the image of the point source, where C_k denotes the region occupied by the k^{th} pixel, and K_{pix} is the number of pixels comprising the image. For a four-plane MUM setup, the images of the distinct focal planes are modeled by

$$\mu_\theta^1(k) = N \cdot \hat{s}_{a^1}^d \left(\frac{x_k}{M} - x_0, \frac{y_k}{M} - y_0, z_{p1} - z_0\right)$$

$$\mu_\theta^2(k) = N \cdot \hat{s}_{a^2}^d \left(\frac{x_k}{M} - x_0, \frac{y_k}{M} - y_0, z_{p2} - z_0\right)$$

$$\mu_\theta^3(k) = N \cdot \hat{s}_{a^3}^d \left(\frac{x_k}{M} - x_0, \frac{y_k}{M} - y_0, z_{p3} - z_0\right)$$

$$\mu_\theta^4(k) = N \cdot \hat{s}_{a^4}^d \left(\frac{x_k}{M} - x_0, \frac{y_k}{M} - y_0, z_{p4} - z_0\right)$$

$k = 1, \cdots, \mathrm{K}_{pix}$, where $\hat{s}_{a^p}^d$ denotes a B-spline of degree d, with continuous representation of the PSF from the perspective of the p^{th} focal plane, calculated directly from a z-stack of an arbitrary NanoGrid hole. The coordinates $(x_k, y_k), k = 1, \cdots, \mathrm{K}_{pix}$, denote the discretized location of the k^{th}image pixel; z_{p1}, z_{p2}, z_{p3}, and z_{p4} denote the positions of the four focal planes in object space; N denotes the total number of point source photons detected in the ROI; and M denotes the lateral magnification of the microscope optics. The parameter vector $\theta = (x_0, y_0, z_0)$ denotes the 3D location of the point source in object space and is estimated by simultaneously fitting the four 3D PSF profiles to the images of the point source using nonlinear least-squares optimization (Figure 3.8) [21]. The images of the point source are first background-subtracted. The background component is assumed to be uniform across all pixels of an image, and its photon contribution is estimated as the median of the intensities of the edge pixels of the images.

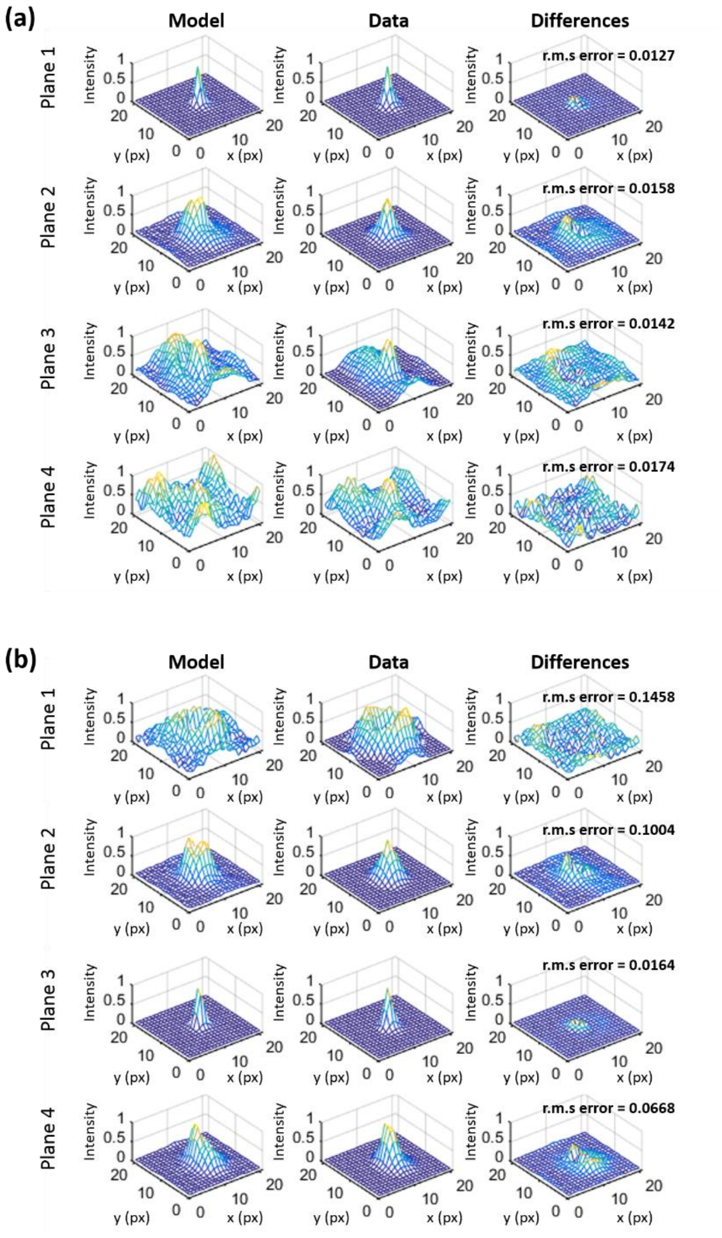

Figure 3.8 Fitting of MUMLA location estimates of a hole acquired using the MUM-module (a) when the estimated z location of the hole is 0.062 μm and (b) when the estimated z location of the hole is -2.538 μm.

The acquired data were processed and analyzed using Lumio (Astero Technologies LLC). The code used for B-spline interpolation was a Java translation of Nathan Cahill's MATLAB code [87].

To validate MUMLA, we moved the MUM-piezo nanopositioner in increments of 200 nm, and at each z position, 20 images of the NanoGrid were acquired per camera (Section 3.2.2). From each set of four frames simultaneously acquired by the four cameras, the images of each NanoGrid hole were simultaneously fitted with four PSF models. These models were obtained by the B-spline interpolation of z-stacks of an arbitrarily chosen NanoGrid hole acquired by the four cameras. For the x-, y-, and z-dimensions, interpolation was performed with smoothing factors 0, 0, and 9, respectively; derivative order 2; and B-spline degree 3. We assume that the focal plane of Camera 1 is the reference focal plane. The position of the reference focal plane is considered to be 0 nm. The positions of the first, second, third, and fourth focal planes are then configured as 0 nm, -1340 nm, -2620 nm, and -3920 nm, respectively (Section 3.2.4).

For the acquired dataset, we estimated the 3D position (i.e., the x, y, and z coordinates) of each hole from a 7 by 7 array of NanoGrid holes at each piezo nanopositioner position (Section 2.2.6). For each hole, the average of the 20 estimated z positions at each piezo nanopositioner position was plotted against the piezo nanopositioner position. The results are shown in the left panel of Figure 3.9. As can be seen, the average z positions of the holes (colored lines) do not match very well with their corresponding piezo nanopositioner positions (black dashed line). Hence, the RMS values of difference between the averaged z positions and their corresponding piezo nanopositioner positions is 178.4 nm. To correct this mismatch, we used MATLAB's "spline" function to generate a cubic spline function by interpolation, using the average of the average z estimates as the independent variable and the piezo nanopositioner positions as the dependent variable. For a given z estimate, we obtained the corrected z position by taking the value of the spline function at the z estimate.

After correction, the average of the corrected z positions matched their corresponding piezo nanopositioner positions closely, as shown in the right panel of Figure 3.9. Here, the RMS values of difference between the averaged z positions and their corresponding piezo nanopositioner positions is 15.3 nm, which is much smaller than the result before correction (178.4 nm). Our results show that the MUM-module can recover the exact step size (200 nm) of the piezo nanopositioner over a depth of 4 μm.

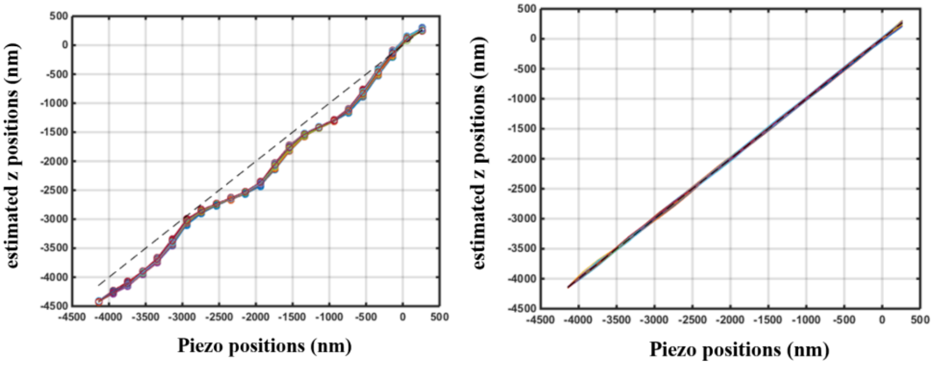

Figure 3.9 Estimated z positions at each piezo nanopositioner position before (left) and after (right) correction.

To evaluate the performance of MUMLA, we used interpolated B-spline PSF models to estimate the 3D positions of an arbitrarily chosen NanoGrid hole (different from the one used to obtain the models). With these, we measured the standard deviation of the x, y, and z position estimates at each piezo nanopositioner position (Figure 3.10). Here, the measured standard deviation is taken to be the localization precision at each piezo nanopositioner position. This measured localization precision was compared to the practical localization accuracy measure (PLAM) [5], which is the best possible localization precision that can be achieved. Computation of the PLAM using the experimental PSF, collectively given by the four B-spline PSF models, was performed using a custom-written software package [88], and the results were plotted against the corresponding positions of the piezo nanopositioner as shown in Figure 3.10. The averages of the absolute differences between the standard deviation and the PLAM for the x, y, and z positions were found to be 1.1, 1.1, and 3.7 nm, respectively. The differences observed may be due to the sample drift that potentially occurred during the sequential acquisition of the repeat images at each piezo nanopositioner position. However, this shows that MUMLA attains the best possible precision in some cases.

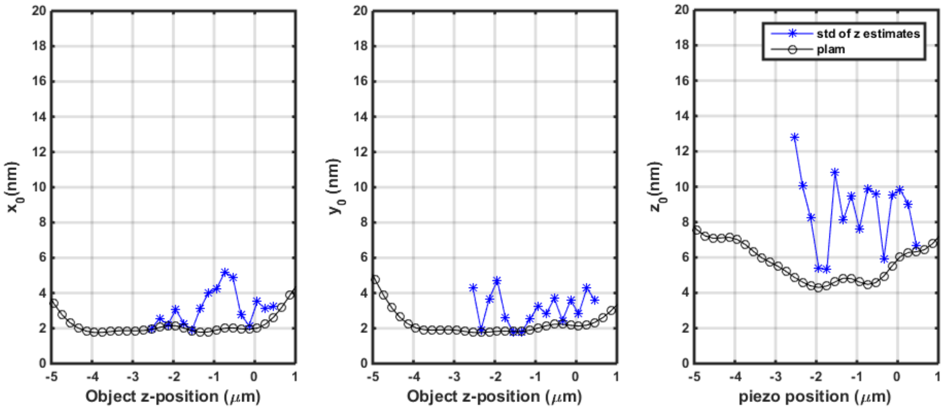

Figure 3.10 Localization precision with respect to the distance from the reference focal plane.

3.3.3. 3D visualization of rMUM calibration data

As a final step, we need to visualize the 3D positions of a single molecule over time (i.e., a single-molecule trajectory), as measured by the MUM-module, overlaid with the 3D volume-rendered image obtained from the r-module. To validate our proposed methods, we first estimated the 3D positions of an array of 7 by 7 holes of NanoGrid at each piezo nanopositioner position from the MUM-module data (Section 2.2.6). The estimated x and y positions of the holes were then registered to the coordinate system in Camera 5 (i.e., r-module) using the transformation matrices generated in Section 3.3.1. Subsequently, 3D volume rendering was performed using the r-module data. The code used for volume rendering was from Oliver Woodford's MATLAB code [89]. This code uses an orthogonal plane 2D texture mapping technique for volume rendering of 3D data in OpenGL. Finally, to avoid overlapping in the volume-rendered image, we overlaid the transformed 3D hole positions (red dots) with the 3D volume-rendered image obtained from the r-module at three chosen piezo nanopositioner positions as shown in Figure 3.11. This figure shows the hole positions (red dots) and the rendered image of the holes completely overlapping each other.

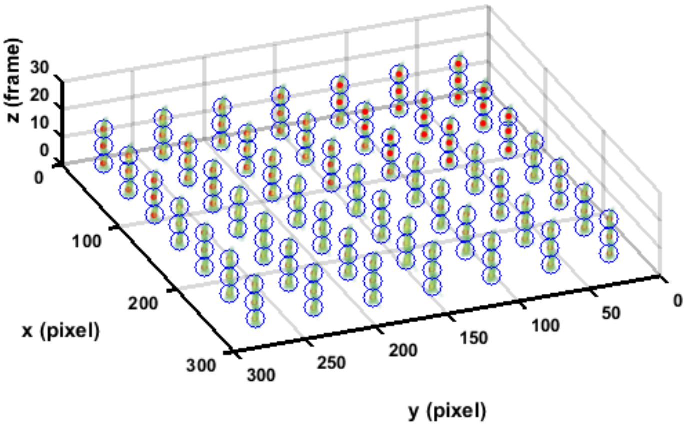

Figure 3.11 Final visualization of the calibration dataset acquired using the rMUM setup.

4. CONCLUSIONS[*]

Single-molecule microscopy has allowed researchers to estimate the location of a single molecule at the nanoscale, which allows tracking individual molecules and visualizing the fine details of subcellular structures. However, significant challenges remain in the analysis, evaluation, and interpretation of single-molecule data in some applications We herein studied different analysis and evaluation techniques of imaging data to study intracellular trafficking that occurs at the level of single molecules.

This dissertation described our two main studies. First, we proposed an approach for calibrating a single-molecule microscope with nanometer level accuracy. This approach is based on the investigation of geometric distortions in light paths by imaging Nanogrid sample, which is made up of regularly spaced apertures. Unlike traditional methods, this technique provided calibration results with an appropriate level of accuracy. We verified our approach with two examples of microscope configurations: a “high-quality” and a “poor-quality” microscope configuration. The results showed that our approach helps detect faulty optical elements in the light path and evaluate single-molecule microscopes. We also proposed an approach for evaluating the quality of optical elements, such as dichroic filters and objective lenses. For the evaluation of dichroic filters, we investigated our approach using dichroic filters with two different types of flatness. The results showed

---

[*] Part of this chapter contains the content of an article that is accepted for publication: S. You, J. Chao, E. A. K. Cohen, R. J. Ober, and E. S. Ward, “A microscope calibration protocol for single-molecule microscopy,” Opt. Express (2020)

the results that the flatness of the dichroic filter may significantly affect the quality of the reflected images. For the evaluation of the objective lenses, we described a methodology for measuring axial chromatic aberrations in objective lenses. These approaches may aid in the calibration of single-molecule microscope systems and help avoid misinterpretations in the multicolor single-molecule imaging data. The proposed calibration method is relatively easy to implement and, therefore, suitable for routine assessments of single-molecule imaging setups in laboratories. By imaging and localizing the sub-wavelength-sized holes of a NanoGrid slide or similar calibration standard, the user can easily follow the protocol to obtain a quality score that quantifies the level of geometric aberration produced by the given imaging configuration. At the core of this method is a general procedure that can be applied not only to the microscope as a whole but also to a specific optical element, as we have demonstrated with dichroic beam splitters.

Second, we demonstrated an approach for optimizing and evaluating rMUM. Unlike traditional imaging systems, this technique helps observe the rapid dynamics of single molecules and helps obtain detailed information on the relevant cellular context. This is important because a single-molecule trajectory alone does not sufficiently explain the biological implications of most subcellular trafficking events. In an rMUM setup, the MUM-module captures the full dynamics of an individual molecule, whereas the r-module acquires z-stack images of the cellular structures with which the molecules interact. Although initial prototypes of rMUM configuration and data analysis has been introduced in the laboratory, performance evaluation and comprehensive data analysis protocols for the imaging systems are still lacking. Hence, to gain a better understanding of subcellular trafficking events, we investigated an approach for optimizing and evaluating imaging experiments with the choice of the correct imaging parameters depending on the application. This method entails a complete experimental pipeline, starting with data acquisition and ending with data analysis and visualization of the obtained events. This protocol enables researchers, from beginners to imaging experts, to utilize rMUM for the study of intracellular trafficking pathways that have been difficult to capture with conventional microscopes and data analysis techniques.

REFERENCES

1. H. Gest, "The discovery of microorganisms by Robert Hooke and Antoni van Leeuwenhoek, fellows of the Royal Society," Notes Rec. R. Soc. Lond. 58(2), 187–201 (2004).

2. K. M. Dean and A. E. Palmer, "Advances in fluorescence labeling strategies for dynamic cellular imaging," Nat. Chem. Biol. 10(7), 512–523 (2014).

3. S. Shashkova and M. C. Leake, "Single-molecule fluorescence microscopy review: shedding new light on old problems," Biosci. Rep. 37(4), BSR20170031 (2017).

4. B. R. Masters, "Ernst Abbe and the foundation of scientific microscopes," Opt. Photonics News 18(2), 18–23 (2007).

5. R. J. Ober, S. Ram, and E. S. Ward, "Localization accuracy in single-molecule microscopy," Biophys. J. 86(2), 1185–1200 (2004).

6. W. E. Moerner and L. Kador, "Optical detection and spectroscopy of single molecules in a solid," Phys. Rev. Lett. 62(21), 2535–2538 (1989).

7. M. Orrit and J. Bernard, "Single pentacene molecules detected by fluorescence excitation in a p-terphenyl crystal," Phys. Rev. Lett. 65(21), 2716–2719 (1990).

8. O. Shimomura, F. H. Johnson, and Y. Saiga, "Extraction, purification and properties of aequorin, a bioluminescent protein from the luminous hydromedusan, aequorea," J. Cell. Comp. Physiol. 59(3), 223–239 (1962).

9. A. Gahlmann and W. E. Moerner, "Exploring bacterial cell biology with single-molecule tracking and super-resolution imaging," Nat. Rev. Microbiol. 12(1), 9–22 (2014).

10. J. A. Cooper, B. R. Mintz, S. L. Palumbo, and W.-J. Li, "Assays for determining cell differentiation in biomaterials," Characterization of Biomaterials 101–137 (2013).

11. D. Axelrod, D. E. Koppel, J. Schlessinger, E. Elson, and W. W. Webb, "Mobility measurement by analysis of fluorescence photobleaching recovery kinetics," Biophys. J. 16(9), 1055–1069 (1976).

12. E. S. Ward and R. J. Ober, "Targeting FcRn to generate antibody-based therapeutics," Trends Pharmacol. Sci. 39(10), 892–904 (2018).

13. R. J. Ober, C. Martinez, X. Lai, J. Zhou, and E. S. Ward, "Exocytosis of IgG as

mediated by the receptor, FcRn: An analysis at the single-molecule level," Proc. Natl. Acad. Sci. 101(30), 11076–11081 (2004).

14. R. J. Ober, C. Martinez, C. Vaccaro, J. Zhou, and E. S. Ward, "Visualizing the site and dynamics of IgG salvage by the MHC class I-related receptor, FcRn," J. Immunol. 172(4), 2021–2029 (2004).

15. P. Prabhat, Z. Gan, J. Chao, S. Ram, C. Vaccaro, S. Gibbons, R. J. Ober, and E. S. Ward, "Elucidation of intracellular recycling pathways leading to exocytosis of the Fc receptor, FcRn, by using multifocal plane microscopy," Proc. Natl. Acad. Sci. 104(14), 5889–5894 (2007).

16. C. Eggeling, J. Widengren, R. Rigler, and C. A. M. Seidel, "Photobleaching of fluorescent dyes under conditions used for single-molecule detection: evidence of two-step photolysis," Anal. Chem. 70(13), 2651–2659 (1998).

17. T. Bernas, M. Zarebski, R. R. Cook, and J. W. Dobrucki, "Minimizing photobleaching during confocal microscopy of fluorescent probes bound to chromatin: role of anoxia and photon flux," J. Microsc. 215(3), 281–296 (2004).

18. A. P. Alivisatos, W. Gu, and C. Larabell, "Quantum dots as cellular probes," Annu. Rev. Biomed. Eng. 7(1), 55–76 (2005).

19. S. F. Lee and M. A. Osborne, "Brightening, blinking, bluing and bleaching in the life of a quantum dot: friend or foe?," ChemPhysChem 10(13), 2174–2191 (2009).

20. I. L. Medintz, H. T. Uyeda, E. R. Goldman, and H. Mattoussi, "Quantum dot bioconjugates for imaging, labelling and sensing," Nat. Mater. 4(6), 435–446 (2005).

21. A. V. Abraham, S. Ram, J. Chao, E. S. Ward, and R. J. Ober, "Quantitative study of single molecule location estimation techniques," Opt. Express 17(26), 23352–23373 (2009).

22. D. Ernst and J. Köhler, "Measuring a diffusion coefficient by single-particle tracking: statistical analysis of experimental mean squared displacement curves," Phys. Chem. Chem. Phys. 15(3), 845–849 (2013).

23. T. C. Rösch, L. M. Oviedo-Bocanegra, G. Fritz, and P. L. Graumann, "SMTracker: a tool for quantitative analysis, exploration and visualization of single-molecule tracking data reveals highly dynamic binding of B. subtilis global repressor AbrB throughout the genome," Sci. Rep. 8(1), 15747 (2018).

24. X. Michalet and A. J. Berglund, "Optimal diffusion coefficient estimation in single-particle tracking," Phys. Rev. E 85(6), 061916 (2012).

25. P. J. Bosch, J. S. Kanger, and V. Subramaniam, "Classification of dynamical diffusion states in single molecule tracking microscopy," Biophys. J. 107(3), 588–598 (2014).

26. L. T. Hall, G. C. G. Beart, E. A. Thomas, D. A. Simpson, L. P. McGuinness, J. H. Cole, J. H. Manton, R. E. Scholten, F. Jelezko, J. Wrachtrup, S. Petrou, and L. C. L. Hollenberg, "High spatial and temporal resolution wide-field imaging of neuron activity using quantum NV-diamond," Sci. Rep. 2(1), 401 (2012).

27. V. Ntziachristos, "Fluorescence molecular imaging," Annu. Rev. Biomed. Eng. 8(1), 1–33 (2006).

28. B. Mandracchia, X. Hua, C. Guo, J. Son, T. Urner, and S. Jia, "Fast and accurate sCMOS noise correction for fluorescence microscopy," Nat. Commun. 11(1), 94 (2020).

29. J. Chao, S. Ram, E. S. Ward, and R. J. Ober, "Ultrahigh accuracy imaging modality for super-localization microscopy," Nat. Methods 10(4), 335–338 (2013).

30. M. J. Sanderson, I. Smith, I. Parker, and M. D. Bootman, "Fluorescence microscopy," Cold Spring Harb. Protoc. 2014(10), pdb.top071795 (2014).

31. D. Axelrod, "Cell-substrate contacts illuminated by total internal reflection fluorescence.," J. Cell Biol. 89(1), 141–145 (1981).

32. D. Axelrod, " Total internal reflection fluorescence microscopy in cell biology," Traffic 2(11), 764–774 (2001).

33. H. P. Kao and A. S. Verkman, "Tracking of single fluorescent particles in three dimensions: use of cylindrical optics to encode particle position," Biophys. J. 67(3), 1291–1300 (1994).

34. L. Holtzer, T. Meckel, and T. Schmidt, "Nanometric three-dimensional tracking of individual quantum dots in cells," Appl. Phys. Lett. 90(5), 053902 (2007).

35. S. R. P. Pavani, M. A. Thompson, J. S. Biteen, S. J. Lord, N. Liu, R. J. Twieg, R. Piestun, and W. E. Moerner, "Three-dimensional, single-molecule fluorescence imaging beyond the diffraction limit by using a double-helix point spread function," Proc. Natl. Acad. Sci. 106(9), 2995–2999 (2009).

36. S. R. P. Pavani and R. Piestun, "High-efficiency rotating point spread functions," Opt. Express 16(5), 3484–3489 (2008).

37. S. Ram, P. Prabhat, J. Chao, E. Sally Ward, and R. J. Ober, "High accuracy 3D quantum dot tracking with multifocal plane microscopy for the study of fast intracellular dynamics in live cells," Biophys. J. 95(12), 6025–6043 (2008).

38. S. Ram, D. Kim, R. J. Ober, and E. S. Ward, "3D single molecule tracking with multifocal plane microscopy reveals rapid intercellular transferrin transport at epithelial cell barriers," Biophys. J. 103(7), 1594–1603 (2012).

39. Z. Gan, S. Ram, R. J. Ober, and E. S. Ward, "Using multifocal plane microscopy to reveal novel trafficking processes in the recycling pathway," J. Cell Sci. 126(5), 1176–1188 (2013).

40. P. Prabhat, S. Ram, E. S. Ward, and R. J. Ober, "Simultaneous imaging of different focal planes in fluorescence microscopy for the study of cellular dynamics in three dimensions," IEEE Trans. Nanobioscience 3(4), 237–242 (2004).

41. C. Eggeling, K. I. Willig, S. J. Sahl, and S. W. Hell, "Lens-based fluorescence nanoscopy," Q. Rev. Biophys. 48(2), 178–243 (2015).

42. F. Balzarotti, Y. Eilers, K. C. Gwosch, A. H. Gynnå, V. Westphal, F. D. Stefani, J. Elf, and S. W. Hell, "Nanometer resolution imaging and tracking of fluorescent molecules with minimal photon fluxes," Science 355(6325), 606–612 (2017).

43. J. Gelles, B. J. Schnapp, and M. P. Sheetz, "Tracking kinesin-driven movements with nanometre-scale precision," Nature 331(6155), 450–453 (1988).

44. H. Qian, M. P. Sheetz, and E. L. Elson, "Single particle tracking. Analysis of diffusion and flow in two-dimensional systems," Biophys. J. 60(4), 910–921 (1991).

45. A. D. Corbett, M. Shaw, A. Yacoot, A. Jefferson, L. Schermelleh, T. Wilson, M. Booth, and P. S. Salter, "Microscope calibration using laser written fluorescence," Opt. Express 26(17), 21887 (2018).

46. A. Royon and N. Converset, "Quality control of fluorescence imaging systems," Opt. Photonik 12(2), 22–25 (2017).

47. N. Chenouard, I. Smal, F. de Chaumont, M. Maška, I. F. Sbalzarini, Y. Gong, J. Cardinale, C. Carthel, S. Coraluppi, M. Winter, A. R. Cohen, W. J. Godinez, K. Rohr, Y. Kalaidzidis, L. Liang, J. Duncan, H. Shen, Y. Xu, K. E. G. Magnusson, J. Jaldén, H. M. Blau, P. Paul-Gilloteaux, P. Roudot, C. Kervrann, F. Waharte, J.-Y. Tinevez, S. L. Shorte, J. Willemse, K. Celler, G. P. van Wezel, H.-W. Dan, Y.-S. Tsai, C. O. de Solórzano, J.-C. Olivo-Marin, and E. Meijering, "Objective comparison of particle tracking methods," Nat. Methods 11(3), 281–289 (2014).

48. J. Chao, R. Velmurugan, S. You, D. Kim, E. S. Ward, and R. J. Ober, "Remote focusing multifocal plane microscopy for the imaging of 3D single molecule dynamics with cellular context," Proc SPIE Int Soc Opt Eng., 10070:100700L (2017)

49. D. Kim, "Imaging three-dimensional single molecule dynamics in its cellular context,"

Texas A&M University (2016).

50. M. J. Saxton and K. Jacobson, "Single-particle tracking: applications to membrane dynamics," Annu. Rev. Biophys. Biomol. Struct. 26(1), 373–399 (1997).

51. M. A. Thompson, J. M. Casolari, M. Badieirostami, P. O. Brown, and W. E. Moerner, "Three-dimensional tracking of single mRNA particles in Saccharomyces cerevisiae using a double-helix point spread function," Proc. Natl. Acad. Sci. 107(42), 17864–17871 (2010).

52. J. Lippincott-Schwartz and G. H. Patterson, "Photoactivatable fluorescent proteins for diffraction-limited and super-resolution imaging," Trends Cell Biol. 19(11), 555–565 (2009).

53. E. Betzig, G. H. Patterson, R. Sougrat, O. W. Lindwasser, S. Olenych, J. S. Bonifacino, M. W. Davidson, J. Lippincott-Schwartz, and H. F. Hess, "Imaging intracellular fluorescent proteins at nanometer resolution," Science 313(5793), 1642–1645 (2006).

54. S. J. Sahl, S. W. Hell, and S. Jakobs, "Fluorescence nanoscopy in cell biology," Nat. Rev. Mol. Cell Biol. 18(11), 685–701 (2017).

55. S. T. Hess, T. P. K. Girirajan, and M. D. Mason, "Ultra-high resolution imaging by fluorescence photoactivation localization microscopy," Biophys. J. 91(11), 4258–4272 (2006).

56. J. Chao, E. Sally Ward, and R. J. Ober, "Fisher information theory for parameter estimation in single molecule microscopy: tutorial," J. Opt. Soc. Am. A 33(7), B36–B57 (2016).

57. F. Balzarotti, Y. Eilers, K. C. Gwosch, A. H. Gynnå, V. Westphal, F. D. Stefani, J. Elf, and S. W. Hell, "Nanometer resolution imaging and tracking of fluorescent molecules with minimal photon fluxes," Science 355(6325), 606–612 (2017).

58. S. Niekamp, J. Sung, W. Huynh, G. Bhabha, R. D. Vale, and N. Stuurman, "Nanometer-accuracy distance measurements between fluorophores at the single-molecule level," Proc. Natl. Acad. Sci. 116(10), 4275–4284 (2019).

59. A. Pertsinidis, Y. Zhang, and S. Chu, "Subnanometre single-molecule localization, registration and distance measurements," Nature 466(7306), 647–651 (2010).

60. R. W. Cole, T. Jinadasa, and C. M. Brown, "Measuring and interpreting point spread functions to determine confocal microscope resolution and ensure quality control," Nat. Protoc. 6(12), 1929–1941 (2011).

61. J. Demmerle, C. Innocent, A. J. North, G. Ball, M. Müller, E. Miron, A. Matsuda, I.

M. Dobbie, Y. Markaki, and L. Schermelleh, "Strategic and practical guidelines for successful structured illumination microscopy," Nat. Protoc. 12(5), 988–1010 (2017).

62. J. J. Schmied, A. Gietl, P. Holzmeister, C. Forthmann, C. Steinhauer, T. Dammeyer, and P. Tinnefeld, "Fluorescence and super-resolution standards based on DNA origami," Nat. Methods 9(12), 1133–1134 (2012).
63. M. Raab, I. Jusuk, J. Molle, E. Buhr, B. Bodermann, D. Bergmann, H. Bosse, and P. Tinnefeld, "Using DNA origami nanorulers as traceable distance measurement standards and nanoscopic benchmark structures," Sci. Rep. 8(1), 1780 (2018).
64. A. von Diezmann, M. Y. Lee, M. D. Lew, and W. E. Moerner, "Correcting field-dependent aberrations with nanoscale accuracy in three-dimensional single-molecule localization microscopy," Optica 2(11), 985–993 (2015).
65. A. D. Corbett, M. Shaw, A. Yacoot, A. Jefferson, L. Schermelleh, T. Wilson, M. Booth, and P. S. Salter, "Microscope calibration using laser written fluorescence," Opt. Express 26(17), 21887–21899 (2018).
66. C. R. Copeland, J. Geist, C. D. McGray, V. A. Aksyuk, J. A. Liddle, B. R. Ilic, and S. M. Stavis, "Subnanometer localization accuracy in widefield optical microscopy," Light Sci. Appl. 7(1), 31 (2018).
67. S. T. Low-Nam, K. A. Lidke, P. J. Cutler, R. C. Roovers, P. M. P. van Bergen en Henegouwen, B. S. Wilson, and D. S. Lidke, "ErbB1 dimerization is promoted by domain co-confinement and stabilized by ligand binding," Nat. Struct. Mol. Biol. 18(11), 1244–1249 (2011).
68. A. D. Douglass and R. D. Vale, "Single-molecule microscopy reveals plasma membrane microdomains created by protein-protein networks that exclude or trap signaling molecules in T cells," Cell 121(6), 937–950 (2005).
69. Carl Zeiss Microscopy operating manual, "Double Adapter Duolink" (Carl Zeiss Microscopy, 2014). https://zeiss.widen.net/s/h2h2htkrpg.
70. S. Yazdanfar, K. B. Kenny, K. Tasimi, A. D. Corwin, E. L. Dixon, and R. J. Filkins, "Simple and robust image-based autofocusing for digital microscopy," Opt. Express 16(12), 8670–8677 (2008).
71. J. F. Brenner, B. S. Dew, J. B. Horton, T. King, P. W. Neurath, and W. D. Selles, "An automated microscope for cytologic research a preliminary evaluation.," J. Histochem. Cytochem. 24(1), 100–111 (1976).
72. E. A. K. Cohen and R. J. Ober, "Analysis of point based image registration errors with applications in single molecule microscopy," IEEE Trans. Signal Process. 61(24),

6291–6306 (2013).

73. J.-C. Olivo-Marin, "Extraction of spots in biological images using multiscale products," Pattern Recognit. 35(9), 1989–1996 (2002).

74. A. V Abraham, S. Ram, J. Chao, E. S. Ward, and R. J. Ober, "Quantitative study of single molecule location estimation techniques," Opt. Express 17(26), 23352–23373 (2009).

75. H. Deschout, F. C. Zanacchi, M. Mlodzianoski, A. Diaspro, J. Bewersdorf, S. T. Hess, and K. Braeckmans, "Precisely and accurately localizing single emitters in fluorescence microscopy," Nat. Methods 11(3), 253–266 (2014).

76. A. Yildiz, "Myosin V walks hand-over-hand: single fluorophore imaging with 1.5-nm localization," Science 300(5628), 2061–2065 (2003).

77. A. R. Lowe, J. J. Siegel, P. Kalab, M. Siu, K. Weis, and J. T. Liphardt, "Selectivity mechanism of the nuclear pore complex characterized by single cargo tracking," Nature 467(7315), 600–603 (2010).

78. M. Tokunaga, N. Imamoto, and K. Sakata-Sogawa, "Highly inclined thin illumination enables clear single-molecule imaging in cells," Nat. Methods 5(2), 159–161 (2008).

79. E. J. Botcherby, R. Juškaitis, M. J. Booth, and T. Wilson, "An optical technique for remote focusing in microscopy," Opt. Commun. 281(4), 880–887 (2008).

80. B. P. Bratton and J. W. Shaevitz, "Simple experimental methods for determining the apparent focal shift in a microscope System," PLoS One 10(8), e0134616 (2015).

81. E. A. K. Cohen, D. Kim, and R. J. Ober, "Cramér-Rao lower bound for point based image registration with heteroscedastic error model for application in single molecule microscopy," IEEE Trans. Med. Imaging 34(12), 2632–2644 (2015).

82. M. Born and E. Wolf, Principles of Optics: Electromagnetic Theory of Propagation, Interference and Diffraction of Light (Elsevier, 2013).

83. S. F. Gibson and F. Lanni, "Experimental test of an analytical model of aberration in an oil-immersion objective lens used in three-dimensional light microscopy," J. Opt. Soc. Am. A 9(1), 154–166 (1992).

84. M. Unser, A. Aldroubi, and M. Eden, "B-spline signal processing. I. Theory," IEEE Trans. Signal Process. 41(2), 821–833 (1993).

85. M. Unser, A. Aldroubi, and M. Eden, "B-spline signal processing. II. Efficiency design and applications," IEEE Trans. Signal Process. 41(2), 834–848 (1993).

86. M. Arigovindan, M. Suhling, P. Hunziker, and M. Unser, "Variational image reconstruction from arbitrarily spaced samples: a fast multiresolution spline solution," IEEE Trans. Image Process. 14(4), 450–460 (2005).

87. N. Cahill, "N-Dimensional BSplines," https://www.mathworks.com/matlabcentral/fileexchange/19632-n-dimensional-bsplines.

88. A. Tahmasbi, E. S. Ward, and R. J. Ober, "Determination of localization accuracy based on experimentally acquired image sets: applications to single molecule microscopy," Opt. Express 23(6), 7630–7652 (2015).

89. O. Woodford, "vol3d v2," https://www.mathworks.com/matlabcentral/fileexchange/22940-vol3d-v2.